

Efficiently Cooled Stellar Wind Bubbles in Turbulent Clouds. I. Fractal Theory and Application to Star-forming Clouds

Lachlan Lancaster, Eve C. Ostriker, Jeong-Gyu Kim, and Chang-Goo Kim, Department of Astrophysical Sciences, Princeton University, 4 Ivy Lane, Princeton, NJ 08544, USA; lachlanl@princeton.edu

*Received 2020 December 21; revised 2021 March 31; accepted 2021 April 14; published 2021 June 18

Abstract

Winds from massive stars have velocities of $1000\,\mathrm{km\,s^{-1}}$ or more and produce hot, high-pressure gas when they shock. We develop a theory for the evolution of bubbles driven by the collective winds from star clusters early in their lifetimes, which involves interaction with the turbulent, dense interstellar medium of the surrounding natal molecular cloud. A key feature is the fractal nature of the hot bubble's surface. The large area of this interface with surrounding denser gas strongly enhances energy losses from the hot interior, enabled by turbulent mixing and subsequent cooling at temperatures $T \sim 10^4 - 10^5\,\mathrm{K}$, where radiation is maximally efficient. Due to the extreme cooling, the bubble radius scales differently ($\mathcal{R}_b \propto t^{1/2}$) from the classical Weaver et al. solution and has expansion velocity and momentum lower by factors of $10-10^2$ at given \mathcal{R}_b , with pressure lower by factors of 10^2-10^3 . Our theory explains the weak X-ray emission and low shell expansion velocities of observed sources. We discuss further implications of our theory for observations of the hot bubbles and cooled expanding shells created by stellar winds and for predictions of feedback-regulated star formation in a range of environments. In a companion paper, we validate our theory with a suite of hydrodynamic simulations.

Unified Astronomy Thesaurus concepts: Star formation (1569); Stellar wind bubbles (1635); Stellar winds (1636); Molecular clouds (1072); Star clusters (1567); Young star clusters (1833)

1. Introduction

Star formation is a notoriously inefficient process, with only a few percent of the gas mass in galaxies being converted to stellar mass over the relevant gravitational timescales (e.g., Kennicutt 1998; Krumholz & Tan 2007; Evans et al. 2009; Murray 2011; Lee et al. 2016; Vutisalchavakul et al. 2016; Barnes et al. 2017; Utomo et al. 2018; Kruijssen et al. 2019). This inefficiency is thought to be caused and regulated by feedback from stars that inject mass, momentum, and energy into their surroundings. This injection happens from the scale of protostellar outflows in cores (e.g., Matzner & McKee 2000; Bally 2016; Offner & Chaban 2017), to individual massive stars in their natal clouds (e.g., Rogers & Pittard 2013; Geen et al. 2015b; Haid et al. 2018), to star clusters in galactic disks (e.g., Kim et al. 2013; Hennebelle & Iffrig 2014; Gatto et al. 2017; Kim & Ostriker 2017), with many different processes playing important roles.

On the scale of clouds, feedback is thought to be dominated by energy provided to the interstellar medium (ISM) by massive stars early in their lives (e.g., Krumholz et al. 2019; Chevance et al. 2020b; Girichidis et al. 2020). This energy can take a number of forms: direct radiation pressure (e.g., Wolfire & Cassinelli 1987; Krumholz & Matzner 2009; Raskutti et al. 2016), pressure from warm gas heated by photodissociating/ionizing radiation leading to ionized and neutral outflows (e.g., Whitworth 1979; Franco et al. 1994; Matzner 2002; Kim et al. 2018, 2021), pressure from infrared (IR) radiation created through the reprocessing of the starlight by dust grains (e.g., Thompson et al. 2005; Murray et al. 2010; Skinner & Ostriker 2015), and the direct input of mechanical energy in the form of stellar winds (e.g., Avedisova 1972; Castor et al. 1975; Weaver et al. 1977; Koo & McKee 1992a, 1992b; Vink et al. 2001).

The importance of these mechanisms has been debated in the recent literature, with several observational studies attempting to assess the relative contributions. This includes observations of evolved clusters in the Large Magellanic Cloud (LMC) by Pellegrini et al. (2011), Lopez et al. (2011, 2014), and McLeod et al. (2019), as well as in the Milky Way (Rosen et al. 2014), in nearby "normal" galaxies (Chevance et al. 2020a; McLeod et al. 2020), and in nearby galaxies with more extreme star-forming environments (Levy et al. 2021). The recent works of Olivier et al. (2021) and Barnes et al. (2020) have sought to make the same evaluation but at very early times (in deeply embedded clusters) in the Milky Way.

Prior to these recent empirical studies intercomparing different feedback effects, earlier observations suggested that the X-ray luminosities of nebulae were too low to be explained by standard wind models (Dunne et al. 2003; Townsley et al. 2003, 2006, 2011). Other works sought to explain this deficit (Garcia-Segura et al. 1996; Capriotti & Kozminski 2001; Mackey et al. 2015; Toalá & Arthur 2018; El-Badry et al. 2019), suggesting turbulent mixing and radiative cooling as sinks of energy, and with Harper-Clark & Murray (2009) appealing to the leakage of hot wind gas out of the cloud interior due to turbulence-induced porosity.

In this paper, we present a model for the evolution of bubbles driven by stellar winds in the presence of strong interface cooling, induced by turbulent mixing. Turbulent motions in the hot gas are derived from the kinetic energy of the wind, with Kelvin-Helmholz and other instabilities growing at interfaces with the dense cloud material, itself highly structured owing to background turbulence. Motivated by recent work on turbulent cooling-mixing layers in the context of multiphase galactic winds and the circumgalactic medium (Gronke & Oh 2018; Fielding et al. 2020; Tan et al. 2021), we argue that this cooling can be very strong, removing up to 99% of the injected energy. The cooling is strong enough to make the dominant phase of the bubble evolution momentum driven (i.e., $p \propto t$). Our model therefore differs significantly from the well-known Weaver et al. (1977) solution, which is energy driven ($E \propto t$, with energy conserved interior to the bubble). Building on previous models for momentum-driven winds (Steigman et al. 1975), we derive predictions for the evolution of important quantities such as the bubble's size and expansion rate, the momentum carried by the swept-up gas exterior to the bubble, and the energy and pressure interior to the bubble. Our goals are to characterize the dependence of bubble evolution on input wind power and ambient cloud properties and to explain the physical mechanisms controlling the evolution.

In a companion paper (Lancaster et al. 2021, hereafter Paper II) we present numerical simulations to validate the theory we develop here and to constrain its few free parameters. We also discuss past numerical studies that have explored this subject.

We have, by design, simplified the problem under consideration. Our model ignores the effects of magnetic fields and extended star formation (in both space and time). Real astronomical systems of course have multiple sources of energy and additional physical elements (such as magnetic fields and strong stellar radiation). By tackling a simpler problem, however, we are able to develop a theoretical framework and make quantitative predictions that can be applied to interpret observations of star-forming clouds. We regard this as a valuable first step toward comprehensive understanding of the role of winds within the array of feedback processes.

The structure of this paper is as follows. In Section 2 we lay out the details of our theory for evolution of wind-driven bubbles in the turbulent ISM. In Section 3 we provide a guide to applying our theory in interpreting observations. Finally, we place our work in context in Section 4, and we conclude with a summary of our findings in Section 5.

2. Theory

In this section we briefly review previous analytic theory of stellar wind bubble evolution and then provide an in-depth explanation of our new theory.

2.1. Classical Stellar Wind Bubble

The classical solution for the structure and evolution of the bubble produced by a constant-luminosity wind expanding into a uniform background medium was described by Weaver et al. (1977) (see also, e.g., Avedisova 1972; Castor et al. 1975; McCray & Kafatos 1987). We focus on the pressure-driven (PD) stage of evolution. This stage was traditionally thought to characterize most of the evolution when a wind-blown bubble is produced in a star-forming cloud by a single massive star or cluster. In this evolutionary stage, energy injected by the wind builds up within the expanding bubble's interior, stored in hot gas that is highly overpressured relative to the ambient surrounding cloud. As it expands into the ambient medium, the overpressured bubble performs work on the background medium, accelerating ambient gas and collecting it in a dense shell surrounding the low-density bubble interior. Provided that the bubble expansion is supersonic with respect to ambient gas (always true for the cold gas in giant molecular clouds [GMCs]), the ambient gas is initially shocked to high temperature and then rapidly cools down to condense into the shell that surrounds the hot bubble interior.

Weaver et al. (1977) divide the structure of the solution into four distinct regions:

- (i) free hypersonic wind;
- (ii) shocked stellar wind;
- (iii) shocked, cooled shell of interstellar gas;

(iv) ambient interstellar gas.

This structure is laid out schematically in of Figure 1(a).

Under the assumption that all of the thermal energy created in the leading shock is radiated away while the bubble interior remains nonradiative, the similarity solution for the bubble radius is

$$R = R_{\rm W}(t) \equiv \left(\frac{125}{154\pi}\right)^{1/5} \left(\frac{\mathcal{L}_{\rm w}t^3}{\bar{\rho}}\right)^{1/5},\tag{1}$$

where \mathcal{L}_w is the wind luminosity, $\bar{\rho}$ is the mass density of the background, and t is the time. We use the "W" subscript to denote the Weaver solution. The dimensionless prefactor is approximately 0.76. During a short-lived earlier stage before the shocked ambient gas cools (analogous to the Sedov–Taylor stage of a supernova remnant), the self-similar solution for the outer radius has the same form, but with a dimensionless prefactor 0.88.

The pressure in the shocked stellar wind evolves as

$$P = P_{W}(t) \equiv \frac{5}{22\pi} \left(\frac{125}{154\pi}\right)^{-3/5} \left(\frac{\mathcal{L}_{w}^{2} \bar{\rho}^{3}}{t^{4}}\right)^{1/5}.$$
 (2)

In the PD bubble solution, the radial momentum carried by the shell¹ is given by

$$p_r = p_{\rm W}(t) \equiv \frac{4\pi}{5} \left(\frac{125}{154\pi}\right)^{4/5} (\mathcal{L}_{\rm w}^4 \bar{\rho} t^7)^{1/5}.$$
 (3)

Of the total wind energy $\mathcal{L}_{w}t$ emitted up to time t, nearly half (45%) is stored in thermal energy in the bubble interior:

$$E_{\text{th,W}} = \frac{3}{2} P_{\text{W}} V_{\text{W}} = \frac{5}{11} \mathcal{L}_{\text{w}} t,$$
 (4)

where $V_{\rm W}$ is the volume of the bubble in this solution. Meanwhile, a much smaller fraction (19%) has gone into the kinetic energy of the swept-up shell

$$E_{\rm kin,W} = \frac{1}{2} M_{\rm sh} \left(\frac{dR_{\rm W}}{dt} \right)^2 = \frac{15}{77} \mathcal{L}_{\rm w} t, \tag{5}$$

where $M_{\rm sh}=4\pi\bar{\rho}R^3/3$ assuming that all the swept-up gas is concentrated in the shell. The remaining $27/77\approx35\%$ of the wind energy is presumed to be radiated away from ISM gas that was shocked as it was swept into the advancing front of the bubble, and then cooled efficiently at high density. It is important to note that in the simplest version of the PD bubble solution, radiative cooling *only* occurs for post-shock, swept-up ISM gas. However, Weaver et al. (1977) do also discuss late-stage evolution when the interior of the bubble drops to low enough temperature that it becomes radiative.

2.2. Pressure-driven Bubble with Interface Cooling

It is widely appreciated that it is difficult to maintain an idealized contact discontinuity, as exists in the classical PD bubble solution, between hot, diffuse gas in the bubble interior (shocked wind) and cool, dense gas of the shell surrounding it (swept-up ISM; e.g., Garcia-Segura et al. 1996;

Throughout this work we will treat the total radial momentum of a given solution as synonymous with the radial momentum in the swept-up shell, as the momentum in the bubble interior is negligible.

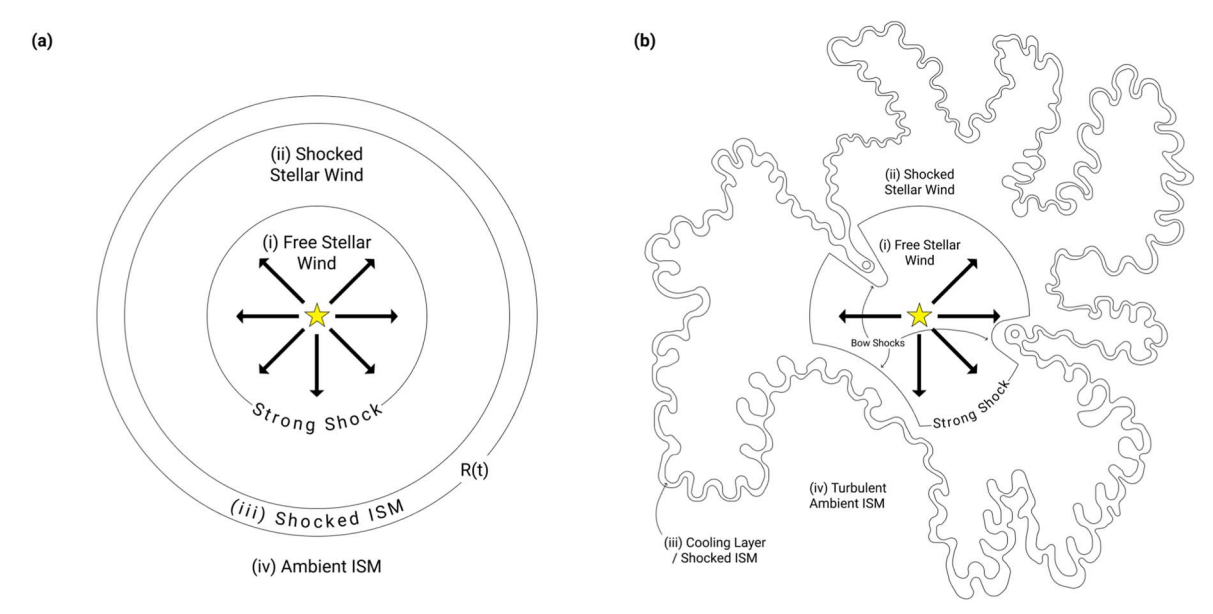


Figure 1. Schematic diagrams illustrating the structure of an expanding wind-driven bubble for (a) the classical PD bubble of Weaver et al. (1977), with a uniform background and cooling only at the leading shock, and (b) the case explored in the present work, where the background is a turbulent medium and there is efficient cooling at the interface between the wind and the shell. For both, the innermost region (i) is the same, consisting of a free-flowing (hypersonic) radial stellar wind. In both cases, there is strong shock in which much of the wind's kinetic energy is thermalized; outside of this is region (ii), consisting of hot, shocked stellar wind. Both phases of the stellar wind have low density and minimal cooling. In panel (b), dense clumps of gas create bow shocks that increase the overall obliquity of the shock front, so that the post-shock radial velocity remains higher. In panel (a), there is a contact discontinuity (and an evaporative flow, if conduction is included) at the interface between the shocked wind and the surrounding dense shell. In panel (b), the shocked wind flows into the dense shell, interacting strongly in a turbulent interface layer, which has a fractal structure. The intermediate-temperature mixture of hot shocked wind gas and dense shell gas cools rapidly and merges into the shell. In both panels (a) and (b), most of the mass in the shell consists of shocked ISM gas that has cooled down. The outermost region (iv) is ambient ISM gas, uniform in panel (a) but turbulent and inhomogeneous in panel (b). Image credit: Cameron Lancaster.

Capriotti & Kozminski 2001). Turbulent motions at this interface, arising from ISM turbulence or from nonlinear development of instabilities (e.g., Vishniac 1983, 1994; Vishniac & Ryu 1989; Blondin et al. 1998; Bucciantini et al. 2004; Folini & Walder 2006; Ntormousi et al. 2011; Michaut et al. 2012; Sano et al. 2012; Pittard 2013; Badjin et al. 2016), will mix together the hot and cool gas. Given the efficiency of cooling at the resulting intermediate temperatures, most of the energy carried into the interface by the hot gas would be radiatively cooled away.

El-Badry et al. (2019) used this fact to derive a simple modification to the PD bubble evolution for the case in which a fraction θ of the wind luminosity is lost to radiation owing to turbulent mixing at the interface between the hot interior and the dense shell of the bubble:

$$\theta \equiv \frac{\mathcal{L}_{\text{int}}}{\mathcal{L}_{\text{w}}},\tag{6}$$

where \mathcal{L}_{int} denotes the total radiative loss from the interface. Allowing for these losses, and assuming that θ is constant in time, the overall bubble evolution follows the same form as in Equations (1)–(5) with the substitution $\mathcal{L}_{w} \to (1-\theta)\mathcal{L}_{w}$. This solution has the same dependence that the Weaver solution has on all of the relevant parameters. For example, the shell radius and outward radial momentum would follow

$$R_{\rm EB}(t) \equiv \left(\frac{125}{154\pi}\right)^{1/5} \left(\frac{\mathcal{L}_{\rm w}(1-\theta)t^3}{\bar{\rho}}\right)^{1/5} \tag{7a}$$

$$p_{\rm EB}(t) \equiv \frac{4\pi}{5} \left(\frac{125}{154\pi}\right)^{4/5} [(1-\theta)^4 \mathcal{L}_{\rm w}^4 \bar{\rho} t^7]^{1/5}.$$
 (7b)

We note that, physically, the bubble expansion is still assumed to be primarily driven by the thermal pressure of the interior, just at a reduced rate.

The interface cooling, \mathcal{L}_{int} , is quite distinct from the energy that is lost to radiation as shocked ISM gas cools down and joins the outside of the shell. In the El-Badry et al. (2019) solution, the radiative losses at the leading shock become $(27/77)(1-\theta)\mathcal{L}_w$, i.e., the same fraction of "available" energy is still lost to cooling in the swept-up, shocked ISM (region (iii) in Figure 1(a)). To make this distinction more explicit, we will define the total fraction of energy that is lost to radiative cooling as

$$\Theta \equiv \frac{\dot{E}_{\text{cool}}}{\mathcal{L}_{\text{w}}}.$$
 (8)

For the El-Badry et al. (2019) solution, $\Theta = 0.35 + 0.65\theta$ and thus² $1 - \Theta = 0.65(1 - \theta)$.

El-Badry et al. (2019) evaluated θ in the case where the mixing is governed by an effective turbulent diffusivity $\kappa_{\rm eff} = \lambda \delta v$, where the right-hand side represents the product of a spatial (λ) and velocity (δv) scale of turbulence in the mixing layer. Since the simulations were spherical, $\kappa_{\rm eff} = \lambda \delta v$ was treated as an arbitrary parameter, and a range of values were explored.

Based on a combination of predicted scaling relations and numerical measurements, El-Badry et al. (2019) showed that θ depends on the ambient medium density $\bar{\rho}$ and cooling rate

Here we use 0.65 (0.35) as approximate shorthand for 50/77 (27/77).

 $\Lambda(T_{\rm pk})$ at the temperature of maximal cooling, $T_{\rm pk}$, as

$$\frac{\theta}{1-\theta} \approx (\kappa_{\rm eff} \bar{\rho})^{1/2} \left[\frac{\Lambda(T_{\rm pk})}{(k_{\rm B} T_{\rm pk})^2} \right]^{1/2},\tag{9}$$

where k_B is the Boltzmann constant.

The pressure is relatively constant in a mixing/cooling interface, but the temperature varies. It is useful to define the minimum cooling time as

$$t_{\text{cool}} \equiv \frac{P}{n^2 \Lambda(T_{\text{pk}})} = \frac{(k_{\text{B}} T_{\text{pk}})^2}{P \Lambda(T_{\text{pk}})}.$$
 (10)

It is straightforward to show that Equation (9) is equivalent to $\theta/(1-\theta)\approx 1.1(\kappa_{\rm eff}/t_{\rm cool})^{1/2}/\dot{R}_{\rm EB}$ for the modified PD bubble solution.

We further note that the El-Badry et al. (2019) simulations included classical microphysical ("Spitzer") thermal conduction in addition to turbulent diffusivity. As discussed in that paper (following Weaver et al. 1977), nonzero thermal conduction leads to evaporation of gas from the interface into the hot interior, which results in an increase of the hot-gas mass and a decrease of its temperature (with pressure unchanged).³ The thermal conduction does not lead to significant cooling because the conduction is only important at high temperatures when cooling is weak. The cooling that does occur is a result of turbulent mixing.

2.3. The Efficiently Cooled (EC) Solution

We now suppose that the energy losses in the bubble/shell interface are so extreme that the PD regime is no longer relevant. A schematic of this scenario is given in Figure 1(b). In this limit, the mixing (and subsequent radiative cooling) of the shocked wind and dense shell gas is extremely efficient, so that little or no energy builds up in the interior of the bubble. When cooling is maximal, only momentum conservation need be considered. We adopt the term "efficiently cooled" (EC) to describe the solution in this limit.

Given a constant mechanical luminosity \mathcal{L}_w and mass-loss rate \dot{M}_w , the wind has asymptotic velocity \mathcal{V}_w and momentum input rate \dot{p}_w given by

$$\mathcal{V}_{\mathbf{w}} \equiv \left(\frac{2\mathcal{L}_{\mathbf{w}}}{\dot{M}_{\mathbf{w}}}\right)^{1/2} \tag{11}$$

and

$$\dot{p}_{\rm w} \equiv \mathcal{V}_{\rm w} \dot{M}_{\rm w} = 2\mathcal{L}_{\rm w} / \mathcal{V}_{\rm w} = (2\mathcal{L}_{\rm w} \dot{M}_{\rm w})^{1/2}. \tag{12}$$

These parameters fully determine the fluid variables in the free wind (section (i) of Figure 1(b)). For the shocked wind (section (ii) of Figure 1(b)), in the Appendix we assume a steady subsonic radial flow to evaluate the fluid variables.

In the limit that no energy is able to build up within the wind bubble, the momentum evolution of the shell surrounding the bubble is entirely determined by the input momentum $\dot{p}_{\rm w}$. In reality, the actual momentum can be somewhat larger than the input wind momentum, though we expect these deviations to

be small. We parameterize any enhancement via a "momentum enhancement factor" α_p (the fundamental free parameter of our theory) and write the momentum equation as

$$\frac{d}{dt}(M_{\rm sh}\langle v_r \rangle) = \alpha_p \dot{p}_{\rm w}, \tag{13}$$

where $M_{\rm sh}$ is the mass swept into a shell by the expanding bubble from the ambient ISM and $\langle v_r \rangle$ is the mass-weighted average radial velocity of that swept-up gas. Assuming that α_p and $\dot{p}_{\rm w}$ are constant in time, the radial momentum of the shell is therefore

$$p_r = \alpha_p p_{\rm EC} \equiv \alpha_p \dot{p}_{\rm w} t = 2\alpha_p \frac{\mathcal{L}_{\rm w}}{\mathcal{V}_{\rm w}} t, \tag{14}$$

where $p_{\rm EC}$ is the result for the case when $\alpha_p = 1$, when cooling is maximally efficient.

It is reasonable to assume, given the statistical homogeneity of the turbulent background mass density field, that the sweptup mass is approximately the product of the volume of the bubble and the mean background density

$$M_{\rm sh} \approx V_b \bar{\rho}.$$
 (15)

Given the statistical isotropy of the background turbulence, it is also reasonable to assume that $\langle v_r \rangle$ is mainly dependent on the rate of change of the bubble volume and not on its specific geometry. To this end we define the bubble's "effective radius" as

$$\mathcal{R}_b \equiv \left(\frac{3V_b}{4\pi}\right)^{1/3} \tag{16}$$

and assume that

$$\langle v_r \rangle \approx \frac{d\mathcal{R}_b}{dt}.$$
 (17)

The deviations from equality in Equations (15) and (17) are essentially geometric and mostly driven by the inhomogeneity and anisotropy of the surrounding gas. For example, the bubble might preferentially expand in directions where the ambient gas has lower density, so that $M_{\rm sh} < V_b \bar{\rho}$.

We now rewrite Equation (13) as

$$\frac{d}{dt} \left(\frac{4\pi}{3} \bar{\rho} \mathcal{R}_b^3 \frac{d\mathcal{R}_b}{dt} \right) = \alpha_R \alpha_p \dot{p}_w \tag{18}$$

where α_R is an order-unity parameter that accounts for any departure from equality in Equations (15) and (17). We note that, unlike the case for other parameters related to energy (see below), there is not a direct relationship between α_R and α_p . However, as we show in Paper II, α_R is very close to 1 for our simulated bubbles. Taking α_R to be approximately constant, Equation (18) can be integrated to obtain

$$\mathcal{R}_b(t) = \left(\frac{3\alpha_R \alpha_p}{2\pi} \frac{\dot{p}_{\rm w} t^2}{\bar{\rho}}\right)^{1/4} \equiv (\alpha_R \alpha_p)^{1/4} R_{\rm EC}. \tag{19}$$

Here $R_{\rm EC}$ denotes the solution for an exactly spherical bubble expanding in a uniform ambient medium when the shell momentum is taken to increase at a constant rate $\dot{p}_{\rm w}$, as has been derived by many authors (e.g., Steigman et al. 1975; Koo & McKee 1992a, 1992b; Kim et al. 2017); this would

³ Ablation (by conduction or Kelvin–Helmholz instabilities) of clouds that have been shocked and overtaken by the expanding high-velocity wind bubble can also add mass to the hot gas (e.g., Cowie & McKee 1977; Klein et al. 1994; Scannapieco & Brüggen 2015; Schneider & Robertson 2017; Gronke & Oh 2018).

apply in the limit of no energy buildup within the bubble interior.

We now wish to determine the energetics of the bubble interior. In the Appendix we give a derivation of the expected values for the fluid variables in the bubble interior under the assumption of spherical geometry with a perpendicular shock dividing the free wind from the post-shock subsonic, steady, radial downstream flow.

Under these assumptions the energy of the bubble interior can be expressed as

$$E_b = \frac{1}{2} \dot{p}_{w} \mathcal{S} \mathcal{R}_b = (\alpha_R \alpha_p)^{1/4} \mathcal{S} E_{b, \text{EC}}.$$
 (20)

Here $E_{b,\mathrm{EC}} = \dot{p}_{\mathrm{w}} R_{\mathrm{EC}}/2$ is the bubble energy in the case where the bubble is occupied solely by the free wind, with $\mathcal{S} = \alpha_p = 1$. More generally, \mathcal{S} encodes the extra energy contained within the bubble ($\mathcal{S} > 1$ when $\alpha_p > 1$), with Equations (A16) and (A13) relating \mathcal{S} to α_p . \mathcal{S} is approximately linear in α_p , with $\mathcal{S} \approx \alpha_p$ within 6%.

The pressure in the shocked wind is nearly constant, equal to its immediate post-shock value, $3\dot{p}_{\rm w}/(16\pi\mathcal{R}_{\rm f}^2)$, where $\mathcal{R}_{\rm f}$ is the outer radius of the free wind region, defined analogously to Equation (16). Written in terms of \mathcal{R}_b and α_p , this is

$$P_b = \frac{3\dot{p}_{\rm w}}{16\pi\mathcal{R}_b^2} \left[\frac{2}{3}\alpha_p + \left(\left(\frac{2}{3}\alpha_p \right)^2 - \frac{1}{3} \right)^{1/2} \right],\tag{21}$$

where the term in square brackets is $\approx (3\alpha_p - 1)/2$ within 4% for the range $1 \le \alpha_p \le 4$ we find in Paper II.

We now consider the kinetic energy of the shell driven by the bubble. If we assume that the vast majority of the input momentum at any time is stored in the shell, we may write its radial kinetic energy as

$$E_{r,sh} = \frac{p_r^2}{2M_{sh}} = \frac{3(\alpha_p \dot{p}_w t)^2}{8\pi\bar{\rho}\mathcal{R}_b^3} = \frac{\alpha_p}{4\alpha_R} \dot{p}_w \mathcal{R}_b.$$
 (22)

The ratio of the bubble interior's energy to the radial kinetic energy of the shell is only weakly dependent on time as

$$\frac{E_b}{E_{r,\text{sh}}} = 2\frac{\alpha_R}{\alpha_p} \mathcal{S},\tag{23}$$

which should be approximately 2 since $S \approx \alpha_p$ and $\alpha_R \sim 1$. This can be compared to the ratio between Equations (4) and (5), which is equal to 7/3 = 2.3. Thus, even though the EC solution has two (or more) orders of magnitude lower energy than the Weaver solution because most energy is radiated away, the ratio of interior to shell energy is comparable.

In addition to expanding radially, the shell may also acquire turbulent motion, such that $E_{\rm sh}=E_{\rm r,sh}+E_{\rm turb,sh}$ is its total kinetic energy. This shell turbulence is a side effect of the interface instabilities that induce mixing and cooling. There is no a priori prediction for the turbulent energy, but we can describe the level of turbulent energy relative to the radial kinetic energy as

$$f_{\rm turb} \equiv \frac{E_{\rm turb,sh}}{E_{\rm r,sh}}.$$
 (24)

With this definition, the total energy of the shell plus bubble interior (neglecting the small thermal energy of the shell) will be $E_{\rm sh} + E_b = (1 + f_{\rm turb} + 2\alpha_R \mathcal{S}/\alpha_p) E_{\rm r,sh}$.

We can use the above to formulate an expression for the fraction of the energy input rate lost to cooling, Θ . From conservation of energy, the energy that is *not* lost to cooling is $\mathcal{L}_{\rm w} \int (1-\Theta)dt$, and this must be equal to $E_{\rm sh}+E_b$. Using Equations (12) and (22) and taking a derivative in time, we obtain

$$1 - \Theta = \left(\frac{1}{2}(1 + f_{\text{turb}})\frac{\alpha_p}{\alpha_R} + \mathcal{S}\right)\frac{\dot{\mathcal{R}}_b}{\mathcal{V}_w}.$$
 (25)

Evidently, because $\dot{\mathcal{R}}_b \propto t^{-1/2}$, the fraction of energy available after cooling is expected to be initially large but decreasing in time. Correspondingly, the fraction Θ of energy lost to cooling is expected to be initially small but increasing with time. In the EC solution, the bubble energy increases as $E \propto \mathcal{R}_b \propto t^{1/2}$; this may be contrasted with $E \propto t$ in classical wind-driven bubble solutions.

Since the dimensionless prefactor in Equation (25) is order unity, the fraction of energy retained $(1-\Theta)$ is comparable to the ratio of the shell expansion velocity to the original wind velocity $(\dot{\mathcal{R}}_b/\mathcal{V}_w)$, which we show (in Paper II) drops to $\sim 1\%$ or lower over time for bubbles expanding in the dense environments of star-forming clouds.

Having explained the evolution of the main physical quantities in the EC theory, we illustrate the significant differences between our theory and that of Weaver et al. (1977) (reviewed in Section 2.1) in Figure 2. Specifically, we show the evolution of the bubble's radius (or \mathcal{R}_b in our theory), the velocity and radial momentum carried by the swept-up gas, and the pressure in shocked wind in the bubble's interior. We show results for three different wind strengths (set by $M_* = 10^3$, 10^4 , 10^5 M_{\odot}), considering a cloud with mass $M_{\rm cloud} = 10^5$ M_{\odot} and radius $R_{\rm cloud} = 20$ pc or $R_{\rm cloud} = 2.5$ pc. The mean ambient density for the larger (smaller) cloud is $n_{\rm H} = 86$ cm⁻³ ($n_{\rm H} = 4.4 \times 10^4$ cm⁻³). For all cases the central source has specific luminosity $\mathcal{L}_{\rm w}/M_* =$ $10^{34} \, \mathrm{erg \ s^{-1} \ M_{\odot}^{-1}}$ and specific mass-loss rate of $\dot{M}_{\mathrm{w}}/M_{\ast} =$ 10^{-2.5} Myr⁻¹, based on Starburst99 (Leitherer et al. 1999). As shown below in Figure 3, these values are appropriate for the first \sim 2.5 Myr of star cluster evolution at solar metallicity. We have assumed $\alpha_R = \alpha_p = \mathcal{S} = 1$ for this comparison, so \mathcal{R}_b is equivalent to $R_{\rm EC}$. The difference between our theory and that of Weaver et al. (1977) is striking. In particular, for the radial momentum and interior pressure, the predictions differ by factors of 10-100.

2.4. The Turbulent Diffusivity

We now consider expectations for the properties of the mixing layer and magnitude of the effective diffusivity $\kappa_{\rm eff}$. In general, a mixing/cooling interface layer of thickness $L_{\rm mc}$ must have a balance between diffusion of energy at volumetric rate $\sim \kappa_{\rm eff} P/L_{\rm mc}^2$ and radiative losses at volumetric rate $\sim n^2 \Lambda = P/t_{\rm cool}$ in the mixed gas. For resolved interface layers with a range of $\kappa_{\rm eff}$, El-Badry et al. (2019) numerically evaluated profiles and found $L_{\rm mc} \approx 2(\kappa_{\rm eff} t_{\rm cool})^{1/2}$, consistent with this expectation; this $t_{\rm cool}$ is based on the maximal cooling rate at a given pressure, defined in Equation (10).

If we consider a flow entering a mixing/cooling interface at velocity v_{rel} , it carries an enthalpy flux $(5/2)v_{\text{rel}}P$. This flux

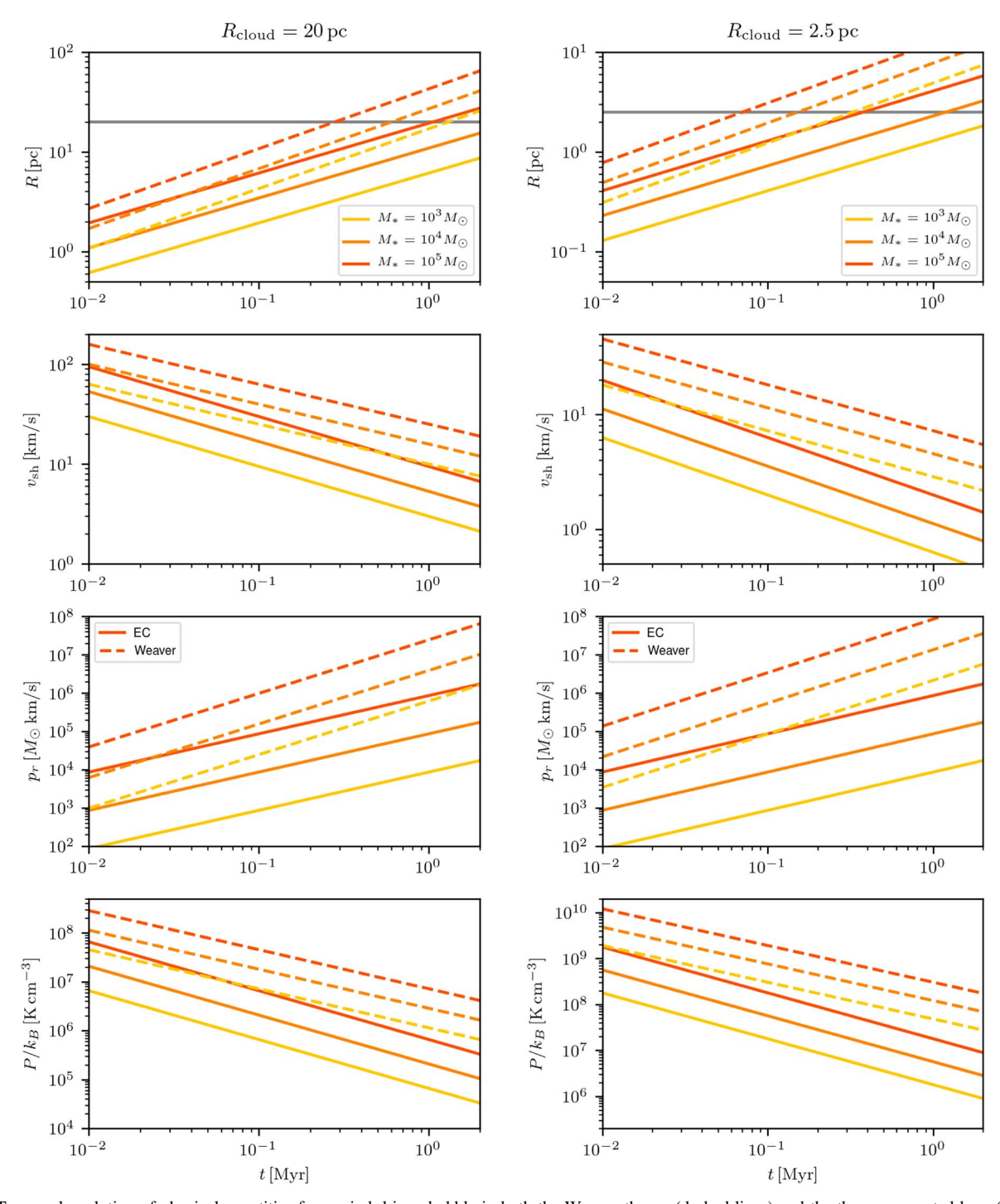


Figure 2. Temporal evolution of physical quantities for a wind-driven bubble in both the Weaver theory (dashed lines) and the theory presented here (solid lines). From top to bottom we show the bubble radius, the velocity and radial momentum of the swept-up gas surrounding the bubble, and the thermal pressure in shocked wind in the bubble interior. We consider a cloud with mass $M_{\text{cloud}} = 10^5 \ M_{\odot}$ and a radius of $R_{\text{cloud}} = 20 \ \text{pc}$ (left panels) or $R_{\text{cloud}} = 2.5 \ \text{pc}$ (right panels). The horizontal gray line in each of the top panels indicates the cloud radius. For every value we explore three different values of the mass of the star cluster driving the wind, $M_* = 10^3$, 10^4 , and $10^5 \ M_{\odot}$ in yellow, orange, and red, respectively.

must be balanced by the cooling per unit area, $n^2 \Lambda L_{\rm mc} = PL_{\rm mc}/t_{\rm cool}$. Equating these rates, we obtain $v_{\rm rel} = (2/5)$ $L_{\rm mc}/t_{\rm cool} \approx 0.8 (\kappa_{\rm eff}/t_{\rm cool})^{1/2}$.

What sets $\kappa_{\rm eff}$? A turbulent boundary layer would in general have a range of physical scales ℓ , with corresponding velocities $v_t(\ell)$. The spectrum of velocity fluctuations is usually assumed

to follow a power law,

$$v_t(\ell) = v_t(L) \left(\frac{\ell}{L}\right)^p, \tag{26}$$

where p is the power-law index of this scaling, L is the largest scale on which this turbulent structure function applies, and $v_t(L)$ is the velocity at that scale.

⁴ Here $v_i(\ell)$ refers to turbulence in the hot gas; Fielding et al. (2020) discuss the relation between turbulent amplitudes in the hot and cool (mixed) gas.

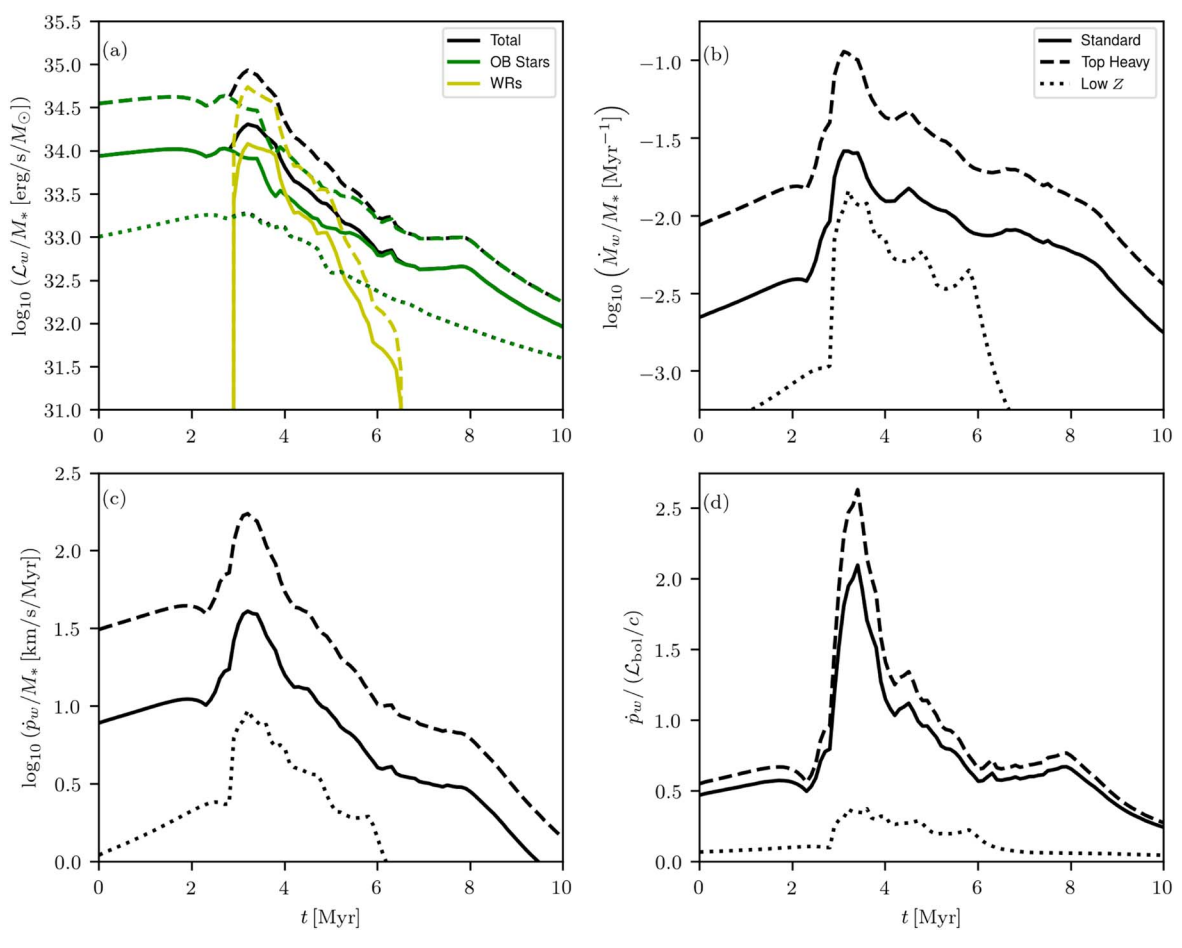


Figure 3. Evolution of several key wind quantities as calculated using the Starburst99 code (Leitherer et al. 1999). We show (a) the wind luminosity per unit mass of the star cluster, (b) the mass-loss rate in the wind per unit stellar mass, (c) the wind momentum injection rate per unit stellar mass, and (d) the ratio of wind momentum input rate to radiation momentum input rate. Solid lines show the result for a standard Kroupa IMF, dashed lines are for a "top-heavy" IMF in which $d \log N/d \log m$ is changed from -2.3 to -1.8 at m > 0.5 M_{\odot} , and dotted lines show the results for a standard IMF but at low metallicity, $Z = Z_{\odot}/7$.

At scale ℓ , the eddy turnover (or flow-crossing) time is

$$t_e(\ell) \equiv \frac{\ell}{v_t(\ell)} = \left(\frac{\ell}{L}\right)^{1-p} \frac{L}{v_t(L)} = \left(\frac{\ell}{L}\right)^{1-p} t_e(L). \tag{27}$$

Since p < 1 in general, $t_e(\ell)$ increases with ℓ . Thus, if the cooling time is short enough that $t_{\rm cool} < t_e(L) = L/v_t(L)$, there always exists some scale $\ell_{\rm cool}$ such that $t_{\rm cool} = t_e(\ell_{\rm cool}) = \ell_{\rm cool}/v_t(\ell_{\rm cool})$ is satisfied. In the language of Tan et al. (2021), this condition is the same as saying that the Damköhler number is greater than 1, which is generally true in our simulations (see Paper II). As noted by Fielding et al. (2020), it is this critical scale, which has $\ell_{\rm cool} = v_t(\ell_{\rm cool})t_{\rm cool}$, that is most relevant for mixing-mediated cooling. Turbulent eddies at $\ell > \ell_{\rm cool}$ will be too slow to directly mix gas in a way that enables rapid cooling, while eddies at $\ell < \ell_{\rm cool}$ will simply further enhance mixing. Thus, the most relevant value for the effective turbulent diffusivity is

$$\kappa_{\text{eff}} = \ell_{\text{cool}} \nu_t(\ell_{\text{cool}}) = t_{\text{cool}} [\nu_t(\ell_{\text{cool}})]^2.$$
 (28)

Using this diffusivity, the thickness of the mixing/cooling layer would be $L_{\rm mc} \approx 2\ell_{\rm cool}$ and the inflow velocity of hot gas

to the interface would be

$$v_{\rm rel} = 0.8 v_t(\ell_{\rm cool}) \approx \frac{\ell_{\rm cool}}{t_{\rm cool}}.$$
 (29)

The scale at which mixing/cooling occurs and the characteristic velocity at that scale can be written in terms of the turbulent properties at the energy-containing scale as

$$\ell_{\text{cool}} = L \left[\frac{v_t(L)t_{\text{cool}}}{L} \right]^{\frac{1}{1-p}}$$
 (30)

and

$$v_t(\ell_{\text{cool}}) = v_t(L) \left[\frac{v_t(L)t_{\text{cool}}}{L} \right]^{\frac{p}{1-p}}.$$
 (31)

The above describe expectations for the turbulent diffusion and the velocity of flow into the interface. In addition to the inflow velocity, the rate of energy loss also depends on the area of the interface. If the main energy-containing scale for the turbulence is L, the interface will be irregular at scales $\lesssim L$. While turbulent mixing and cooling would still lead to inflow to the interface at $v_{\rm rel} \sim v_{\rm f}(\ell_{\rm cool})$, the net cooling is enhanced by having a surface that is highly corrugated at small scales. We turn to this in the next section.

2.5. Fractal Nature of the Turbulent Boundary Layer

In a recent investigation of turbulent, cooling boundary layers driven by Kelvin–Helmholtz instabilities between hot diffuse gas and cool dense gas, Fielding et al. (2020) pointed out that the surface of the interface obeys a fractal scaling law (see also Tan et al. 2021, who connect this to results in the combustion literature). Fielding et al. (2020) used this fractal nature to derive a prediction for the rate of mixing and cooling that occurs at shearing interfaces between cool, dense gas and hot, diffuse gas.

In particular, Fielding et al. (2020) argue that the rate of thermal energy loss to cooling will be equal to the rate at which energy can be simultaneously mixed and cooled into the turbulent interface,

$$\dot{E} pprox rac{5}{2} P v_t(\ell_{
m cool}) A(\ell_{
m cool}),$$

where $A(\ell_{\rm cool})$ is the area of the (fractal) interface at scale 5 $\ell_{\rm cool}$. The above corresponds to the same characteristic inflow velocity of hot gas $v_{\rm rel} \approx v_{\rm f}(\ell_{\rm cool}) = \ell_{\rm cool}/t_{\rm cool}$ as given in Equation (29), while the total cooling rate takes into account the fractal area $A(\ell_{\rm cool})$ of the interface at the scale $\ell_{\rm cool}$. The above relation is valid up to an order-unity constant, which is quantified in Fielding et al. (2020) for the case where the interface is planar on large scales. The coefficient may depend somewhat on the details of the problem (including how turbulence is driven and large-scale geometry), so for present purposes we concentrate on scalings.

For the wind-blown bubble problem, we define an "equivalent" thermal energy flux Φ_{cool} that can be lost to cooling via interface mixing as the rate of energy loss divided by the surface area of an equivalent sphere,

$$\Phi_{\text{cool}} \approx \frac{5}{2} P v_t(\ell_{\text{cool}}) \frac{A_b(r; \ell_{\text{cool}})}{4\pi r^2}.$$
(32)

Here $A_b(r; \ell_{\text{cool}})$ is now the full fractal surface area of the windblown bubble when the bubble has some linear scale (e.g., its radius) r.

We will make the assumption that the thin interface between the shocked wind and the cool shell (i.e., between regions (ii) and (iii) in Figure 1(b)) can be described by a fractal of dimension D > 2 (as it is an interface). We will refer to its "excess dimensionality" as $d \equiv D - 2$.

Physically, this means that if the bubble has an overall linear scale r, the area of the bubble surface measured on scale ℓ will be

$$A_b(r;\ell) \approx 4\pi r^2 \left(\frac{r}{\ell}\right)^d$$
. (33)

As in Section 2.4, we assume that the energy-containing scale of turbulence in hot gas near the interface is L and that the turbulence can be described by a structure function of the form of Equation (26) for $\ell \leq L$. The power-law index is expected to take on a value $p \sim 1/3$ because the turbulence in the hot gas is generally subsonic. The amplitude $v_t(L)$ likely depends primarily on instabilities at the interface since the wind is the main source of free energy, but the background cloud turbulence may be important in seeding them.

Using Equations (30) and (31), the equivalent energy flux is expected to follow

$$\Phi_{\text{cool}} \approx \frac{5}{2} P v_t(\ell_{\text{cool}}) \left(\frac{r}{\ell_{\text{cool}}}\right)^d$$
(34a)

$$\approx \frac{5}{2} P v_t(L) \left(\frac{\ell_{\text{cool}}}{L}\right)^{p-d} \left(\frac{r}{L}\right)^d \tag{34b}$$

$$\approx \frac{5}{2} P v_t(L) \left[\frac{v_t(L) t_{\text{cool}}}{L} \right]^{\frac{p-d}{1-p}} \left(\frac{r}{L} \right)^d.$$
 (34c)

We emphasize that the fractal nature of the interface plays a major role in enhancing energy losses, given by the factor $(r/\ell_{\rm cool})^d$ in Equation (34a). It is important to note that strong inhomogeneity in a cloud (due to preexisting high Mach number turbulence) can make the fractal structure global, with $r \gg L$; from Equation (34c) this strongly enhances cooling.

Fielding et al. (2020) measured $d \approx 1/2$ for the excess dimensionality of the fractal interface in the mixing/cooling layer of their simulations. Combining this with p = 1/3 for subsonic turbulence yields

$$\Phi_{\text{cool}} \approx \frac{5}{2} P v_t(L) \left[\frac{v_t(L) t_{\text{cool}}}{L} \right]^{-1/4} \left(\frac{r}{L} \right)^{1/2}. \tag{35}$$

Since the Fielding et al. (2020) simulations were for a local rectangular box with a shear layer, rather than a global expanding bubble, in the situation they studied $r/L \rightarrow 1$. The predicted scaling $\Phi_{\rm cool} \propto v_t(L)^{3/4} t_{\rm cool}^{-1/4}$ with the measured large-scale turbulent velocity $v_t(L)$ and imposed cooling time $t_{\rm cool}$ were found to be in excellent agreement with numerical results

For present purposes, in order to keep the relation to the spherical case more explicit and use the variables that we have already developed to represent the linear scale of the bubble, we will write the fractal area relation as

$$A_b(\mathcal{R}_b; \ell) \equiv 4\pi\alpha_A \mathcal{R}_b^2 \left(\frac{\mathcal{R}_b}{\ell}\right)^d,$$
 (36)

where α_A is an order-unity constant, which we quantify in Paper II.

Finally, we note that even if a properly calibrated $\kappa_{\rm eff} = v_t(\ell_{\rm cool})\ell_{\rm cool}$ were used and the cooling length were resolved in one-dimensional simulations, it would not be possible to capture the fractal nature of the interface, and hence the total cooling would not be correctly captured. To achieve the proper energy-loss rate, an "area-corrected" effective diffusivity $\kappa_{\rm corr,1D} = v_t(\ell_{\rm cool})\ell_{\rm cool}(r/\ell_{\rm cool})^{2d}$ would have to be adopted instead, where r now denotes the radius of the interface between the hot bubble and ambient medium in the 1D simulation. From Equation (30), this can be written in terms of the energy-containing scale of the turbulence as

$$\kappa_{\text{corr,1D}} = v_t(L) L \left[\frac{v_t(L) t_{\text{cool}}}{L} \right]^{\frac{1+p-2d}{1-p}} \left(\frac{r}{L} \right)^{2d}. \tag{37}$$

2.6. Conditions for Efficient Cooling

Here we analyze the conditions under which a wind can become "efficiently cooled." One such condition could be stated as the point at which the momentum incurred by pressure work, given for the PD bubble with cooling by Equation 7(b),

⁵ Fielding et al. (2020) adopt the notation w for the critical scale that here we denote $\ell_{\rm cool}$.

is less than the direct momentum input from the wind, $\dot{p}_{\rm w}t=p_{\rm EC}$ (Equation (14), which is the total momentum in the EC case). This condition can be expressed formally as

$$1 - \Theta < 4 \left(\frac{5}{6}\right)^{1/4} \frac{\dot{R}_{EC}}{V_{vv}}.$$
 (38)

Since $R_{\rm EC} \propto t^{1/2}$, the term on the right above varies as $t^{-1/2}$. If cooling losses are sufficiently weak, the efficient-cooling condition may be satisfied only at the earliest times. If, however, cooling losses are strong, $1 - \Theta \ll 1$, essentially the whole bubble evolution may be in the efficient-cooling regime.

The above gives us a necessary condition on Θ for the wind to be "efficiently cooled." If an estimate of the cooling losses were known, then this test would decide whether the cooling-modified PD (Section 2.2) or EC (Section 2.3) bubble solution is valid. Since, however, we have no a priori knowledge of Θ (except through Equations (9) and (37)), it is more useful to obtain a physically motivated condition for the EC solution to apply.

To this end, we compare the estimated thermal energy flux that can be lost to cooling at a turbulent interface, $\Phi_{\rm cool}$ (Equation 34(c)), to the thermal energy flux that an unimpeded shocked wind would carry. Immediately after the shock, at radius $\mathcal{R}_{\rm f}$, this flux is $\Phi_{\rm w}\approx (5/2)P_{\rm ps}\nu_{\rm ps}$ with $P_{\rm ps}=3\dot{p}_{\rm w}/(16\pi\mathcal{R}_{\rm f}^2)$ and $\nu_{\rm ps}=\mathcal{V}_{\rm w}/4$ for a spherical shock. Since the pressure is approximately constant in the subsonic post-shock region while energy is conserved (see the Appendix), the energy flux carried into the boundary layer is $\Phi_{\rm w}\approx (5/2)P_{\rm ps}\nu_{\rm ps}(\mathcal{R}_{\rm f}/\mathcal{R}_{\rm b})^2$.

The condition for efficient cooling is that the capacity for mixing/cooling matches or exceeds the rate at which thermal energy is advected to the interface ($\Phi_{\rm w} \lesssim \Phi_{\rm cool}$), which may be expressed as

$$\frac{2}{3\alpha_{p}-1}v_{ps} \lesssim v_{t}(L) \left[\frac{v_{t}(L)t_{cool}}{L}\right]^{\frac{p-d}{1-p}} \left(\frac{\mathcal{R}_{b}}{L}\right)^{d}.$$
 (39)

For the numerical coefficient on the left-hand side we have used the small- α_p approximation given in Equation (A14); when $\alpha_p\gg 1$, the prefactor would instead become $3/(4\alpha_p)$, from Equation (A13). The exponent (p-d)/(1-p) depends on the exact fractal dimension, as well as the power of the turbulent structure function. If $d\approx 1/2$ and $p\approx 1/3$, as previously suggested by Fielding et al. (2020), this exponent is -1/4, but in any case it is likely to be small and negative. Still, $t_{\rm cool}$ can be as small as ~ 10 –100 yr in dense clouds (see Paper II for numerical results). With typical $v_t(L)\sim 0.1\mathcal{V}_w\gtrsim 100~{\rm km~s^{-1}}$ and $L\sim 0.1\mathcal{R}_b\lesssim 1~{\rm pc}$, the efficient-cooling condition is satisfied for a strong shock with $v_{\rm ps}=\mathcal{V}_{\rm w}/4$. Even if oblique shocks yield a larger hot-gas velocity $v_{\rm ps}\lesssim \mathcal{V}_{\rm w}$, the efficient-cooling condition is likely to be at least marginally satisfied.

If we think of Equation (39) as representing an outer boundary condition on the flow within the bubble, it shows that lower turbulence levels will allow for larger α_p , i.e., more buildup of shocked gas within the bubble. Very high turbulence levels and large fractal dimension, in contrast, would lead to extremely efficient mixing, with $\alpha_p \sim 1$.

Finally, we remark that in numerical simulations limited numerical resolution may impose a minimum resolved scale $\ell_{\min} \sim \Delta x$, where $\ell_{\text{cool}} < \ell_{\min} < L$. Following the arguments

leading to Equations (34a)–(34b) and then Equation (39), mixing at ℓ_{min} would provide sufficient cooling for the EC solution to be satisfied provided that

$$\frac{2}{3\alpha_p - 1} v_{\text{ps}} \lesssim v_t(\ell_{\min}) \left(\frac{\mathcal{R}_b}{\ell_{\min}}\right)^d \tag{40a}$$

$$\sim v_t(L) \left(\frac{\ell_{\min}}{L}\right)^{p-d} \left(\frac{\mathcal{R}_b}{L}\right)^d.$$
 (40b)

With $p-d \sim -1/6$, the cooling rate would tend to *increase* as resolution and ℓ_{\min} get smaller. Thus, if Equation (40a) is already satisfied for resolved turbulence at scale ℓ_{\min} of a few Δx , further improvement in the resolution would not alter the behavior given by Equation (19).

In Paper II we use Equation (40a) as an additional check of whether we are in the efficiently cooled regime. However, due to resolution effects, the structure function of the turbulence is often steeper than it should be, meaning that cooling does not necessarily increase with decreasing scale *all the way* to the resolution limit. If the true mixing rate is higher than the rate achieved in our simulations owing to resolution limitations, the EC conditions in reality would be even better satisfied, with α_p even closer to unity.

3. Application to Star-forming Clouds

Here we write down several formulae that will equip the reader to make practical use of our theory. To inform this discussion, we show in Figure 3 the evolution in time of several quantities related to stellar winds as calculated using the Starburst99 code (Leitherer et al. 1999). We show the evolution of the specific wind luminosity, the specific mass-loss rate, the specific momentum input rate, and the so-called "wind efficiency parameter," which is the ratio of momentum input rate in the wind and in radiation, $\dot{p}_{\rm w}/(L_{\rm bol}/c)$.

For all quantities we show the evolution for a standard solar metallicity (Z = 0.014), Kroupa initial mass function (IMF; Kroupa 2001) (solid lines); for a "top-heavy" IMF with a shallower slope at m > 0.5 M_{\odot} and solar metallicity (dashed lines); and for a standard IMF with $Z = 0.002 \approx 10^{-0.85} Z_{\odot}$ (dotted lines, same as "low-Z" models in Leitherer et al. 2014). Additionally, in panel (a) we separately show the contributions from OB stars (green lines), Wolf-Rayet (W-R) stars (yellow lines), and the total (black lines). There are also very minor contributions to the total $\mathcal{L}_{\mathrm{w}}/M_{*}$ from luminous blue variable stars and red supergiant stars. We do not show these separately, but they are included in the displayed total. The choice of the slope for the alternative IMF, $d \log N / d \log m = -1.8$ (instead of -2.3 for the standard IMF), is motivated by observations indicating that super star clusters (SSCs), including those in the Galactic center, may be top-heavy (McCrady et al. 2005; Lu et al. 2013; Hosek et al. 2019).

Our theory, as well as the simulations of Paper II, assumes that all the wind properties are constant in time. Figure 3 shows that this assumption is reasonable during the first \sim 2 Myr of wind evolution, before the onset of significant energy input from W-R stars. For all of the numerical estimates below, we adopt the standard Kroupa IMF. With a top-heavy IMF, $\dot{p}_{\rm w}$ would be a factor of 4 higher, whereas $\dot{p}_{\rm w}$ would be an order of magnitude lower with a low-metallicity IMF.

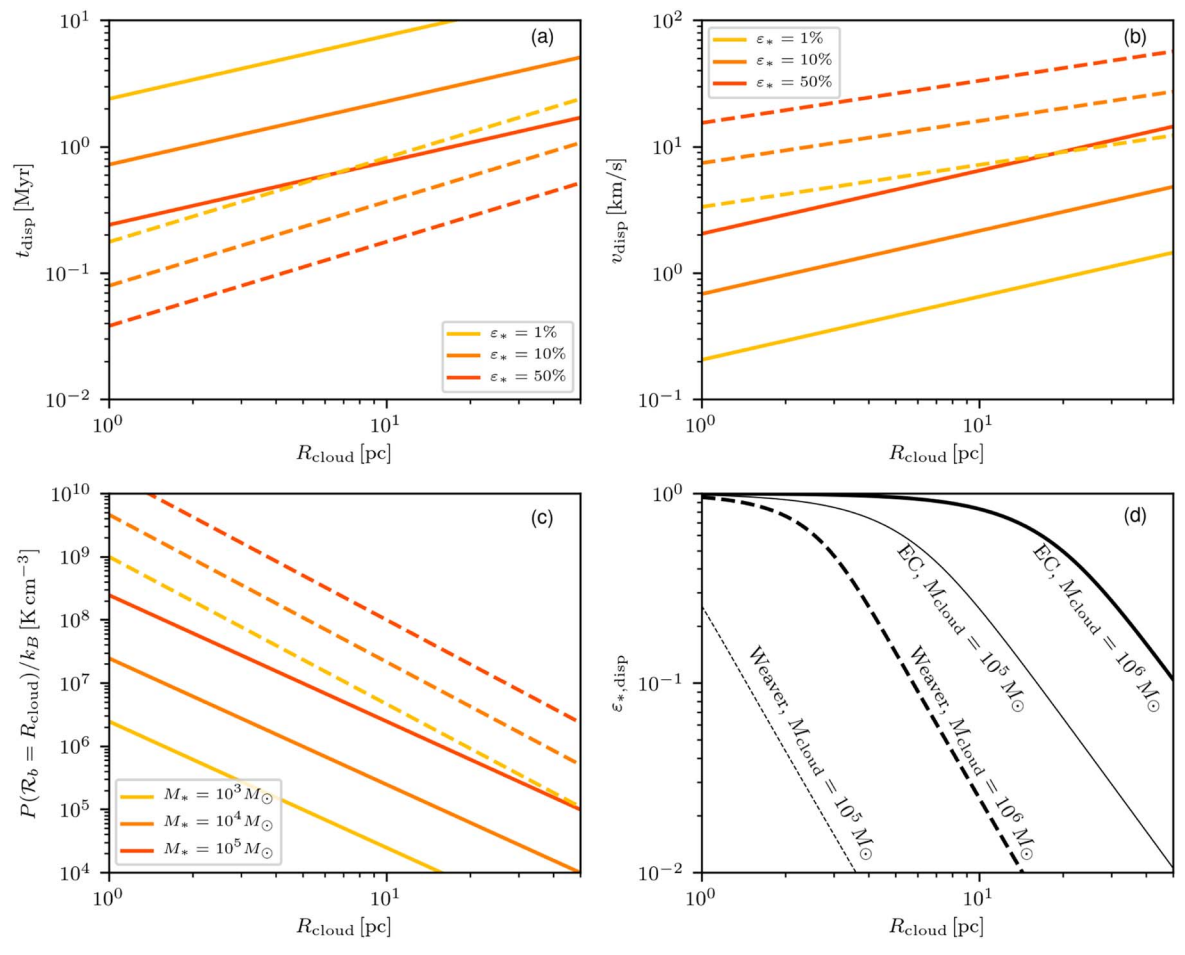


Figure 4. Comparison of several quantities as predicted by our theory (solid lines) and that of Weaver et al. (1977) (dashed lines). For the top two panels we show results as a function of cloud radius and SFE $\varepsilon_* = 1\%$, 10%, and 50%, while the bottom left shows results for $M_* = 10^3$, 10^4 , and $10^5 M_{\odot}$ (yellow, orange, and red, respectively), using $M_{\text{cloud}} = 10^5 M_{\odot}$ for the dashed lines. Panels show (a) shell velocity v_{disp} when the bubble has reached the edge of the cloud, (b) time t_{disp} taken for this to occur, (c) the bubble interior pressure at this time, and (d) the SFE needed to disperse the surrounding cloud. Here we show $\varepsilon_{*,\text{disp}}$ as a function of R_{cloud} for $M_{\text{cloud}} = 10^6$ and $10^5 M_{\odot}$ displayed as the thick and thin lines, respectively.

For the purposes of enabling quick calculations, the formulae we present below are written as simply as possible, setting $f_{\text{turb}} = 0$, $\alpha_R = 1$. Where appropriate, we comment on the range of adjustments that would be expected based on the numerical results presented in Paper II. Additionally, in Figure 4 we provide a comparison of the predictions of our theory and that of Weaver et al. (1977) for several key quantities of interest. As we shall show, the shell velocities, cloud dispersal timescales, and hot-gas pressures in the EC solution can be orders of magnitude below the corresponding values for the Weaver et al. (1977) solution. This also implies that much higher star formation efficiency (SFE) would be required to disperse the cloud when interface cooling is taken into account.

The primary application of our results is to bubbles collectively driven by the winds from young massive stars in clusters within star-forming clouds. We shall take the total stellar mass of the cluster (including both low- and high-mass stars) as M_{\ast} and assume a centrally concentrated wind source. Using the result from SB99 with a standard Kroupa IMF, the direct wind momentum input rate is

$$\dot{p}_{\rm w} = 8.6 \,\rm km \, s^{-1} \, Myr^{-1} M_*;$$
 (41)

here the coefficient is based on an average over the first Myr, while the value would be slightly lower (\approx 7.85) for an average

over 0.1 Myr. Averaging over the same time period, $V_w = 3512 \text{ km s}^{-1}$. Our solution allows for the momentum input rate to be enhanced by a factor α_p relative to the ideal "momentum-conserving" limit (see Equation (14)).

We shall assume that after a time t the gas surrounding the central cluster has been swept up in a shell of mass $M_{\rm sh}$ by the wind. The shell's velocity will then be

$$v_{\rm sh} = 8.6 \,\mathrm{km} \,\mathrm{s}^{-1} \alpha_p \frac{M_*}{M_{\rm sh}} \frac{t}{\mathrm{Myr}}.$$
 (42)

When the input wind power is very low (e.g., $M_* \lesssim 10^3 \, M_\odot$), we show in Paper II that $\alpha_p \sim 1.5-4$. This range could apply in moderate-density GMCs, where the efficiencies of star cluster formation are only $M_*/M_{\rm cloud} \equiv \varepsilon_* \sim 1\%-10\%$ (Lada et al. 2010; Vutisalchavakul et al. 2016). However, winds are likely to be most important relative to other feedback processes in very dense clouds, such as those forming SSCs, where $\varepsilon_* \gtrsim 10\%$ (Leroy et al. 2017; Emig et al. 2020; Levy et al. 2021). For this range, the momentum enhancement above the direct wind input is modest, $\alpha_p \sim 1.2-2$ (see Paper II).

The evolutionary time is difficult to ascertain in observations, but from Equation (19) the shell velocity can also be expressed in terms of its mass $M_{\rm sh}$, radius $R_{\rm sh} = \mathcal{R}_b$, and $\dot{p}_{\rm w}$ as

$$v_{\rm sh} = \left(\frac{\alpha_p \dot{p}_{\rm w}}{2} \frac{R_{\rm sh}}{M_{\rm sh}}\right)^{1/2} \tag{43a}$$

= 2.0 km s⁻¹
$$\left(\alpha_p \frac{M_*}{M_{\rm sh}} \frac{R_{\rm sh}}{1 \text{ pc}}\right)^{1/2}$$
, (43b)

where we have assumed $M_{\rm sh}=4\pi R_{\rm sh}^3 \bar{\rho}/3$. Given that $\alpha_p^{1/2}\sim 1-2$, Equation 43(b) makes clear that a wind-driven shell can only reach velocity >10 km s⁻¹ if $M_*\gg M_{\rm sh}$, assuming that $R_{\rm sh}$ is in the range $\sim 1-25$ pc of observed starforming clouds. We note, however, that a top-heavy IMF would increase the shell momentum and velocity somewhat.

We can also use Equation (19), setting $\mathcal{R}_b = R_{\rm cloud}$, to obtain an estimate for the time required for a wind-driven bubble from an embedded cluster to disperse the entire surrounding parent cloud. For this simple estimate, we set $M_* = \varepsilon_* M_{\rm cloud}$ and $M_{\rm sh} = (1 - \varepsilon_*) M_{\rm cloud}$. The cloud dispersal time can then be written as

$$t_{\rm disp} = \left(\frac{M_*}{2\alpha_p \dot{p}_{\rm w}} \frac{1 - \varepsilon_*}{\varepsilon_*} R_{\rm cloud}\right)^{1/2} \tag{44a}$$

$$= 0.24 \text{ Myr} \left(\frac{1}{\alpha_p} \frac{1 - \varepsilon_*}{\varepsilon_*} \frac{R_{\text{cloud}}}{1 \text{ pc}} \right)^{1/2}. \tag{44b}$$

The shell velocity $v_{\rm disp}$ at this time is obtained by replacing $M_*/M_{\rm sh} \rightarrow \varepsilon_*/(1-\varepsilon_*)$ and $R_{\rm sh} \rightarrow R_{\rm cloud}$ in Equation (43b). It is interesting that these expressions are not (explicitly) dependent on the total cloud mass. As before, the enhancement of the momentum input rate relative to the ideal $(\alpha_p=1)$ EC solution would imply at most a $\sim\!30\%$ reduction in $t_{\rm disp}$ for cases with $\varepsilon_*\gtrsim10\%$. A key point is that compact clouds with high ε_* would be dispersed by wind feedback very rapidly, well before supernovae commence.

It is important to note that the expansion rate and therefore other derived values such as the cloud dispersal time are very different in the EC solution from what they would be if the classical Weaver et al. (1977) solution were applied. For example, using the Weaver et al. (1977) solution, equivalent calculations to the above would instead yield

$$t_{\rm disp,W} = 0.038 \,\mathrm{Myr} \left(\frac{1 - \varepsilon_*}{\varepsilon_*}\right)^{1/3} \left(\frac{R_{\rm cloud}}{1 \,\mathrm{pc}}\right)^{2/3} \tag{45}$$

and

$$v_{\rm disp,W} = 15.4 \text{ km s}^{-1} \left(\frac{\varepsilon_*}{1 - \varepsilon_*}\right)^{1/3} \left(\frac{R_{\rm cloud}}{1 \text{ pc}}\right)^{1/3}$$
 (46)

for the cloud dispersal time and the shell velocity at that time, respectively.

In the top two panels of Figure 4, we compare the EC and Weaver solutions for the breakout time and corresponding velocity. For the EC solution, the breakout velocity (breakout time) is a factor $\sim 5-10$ lower (higher). Since Equation (45) underestimates the dispersal timescale by up to an order of magnitude, we caution against its use. We also caution that the estimates in Weaver et al. (1977) and Mac Low & McCray (1988) of the cooling time for wind-blown bubbles cannot be used to modify the solution of Equation (1), as they are

obtained under the assumption that the hot bubble interior is itself cooling, rather than cooling losses occurring as a result of turbulent mixing at the interface between hot and cool gas.

Our above estimates, and the analysis and simulations of this paper and Paper II more generally, neglect the effects of gravity. In reality, the rate at which the expanding shell gains momentum will be instantaneously reduced by the gravitational force of the cluster on the shell, $GM_*M_{\rm sh}/R_{\rm sh}^2$, and the gravitational force of the shell on itself, $GM_{\rm sh}^2/(2R_{\rm sh}^2)$. Allowing for gravity, the wind can drive expansion only provided that

$$M_{\rm sh} + \frac{M_{\rm sh}^2}{2M_{*}} < \alpha_p \frac{\dot{p}_{\rm w}}{M_{*}} \frac{R_{\rm sh}^2}{G}.$$

For a self-gravitating cloud to be fully dispersed by an expanding wind bubble, we again set $R_{\rm sh} = R_{\rm cloud}$, $M_* = \varepsilon_* M_{\rm cloud}$, and $M_{\rm sh} = (1 - \varepsilon_*) M_{\rm cloud}$ and solve the inequality to obtain a condition on the SFE, ε_* . We express this condition in terms of the original surface density of gas in the cloud, $\Sigma_{\rm cloud} \equiv M_{\rm cloud}/(\pi R_{\rm cloud}^2)$:

$$\frac{1 - \varepsilon_*^2}{\varepsilon_*} < \frac{2\alpha_p}{\pi} \frac{\dot{p}_{\rm w}}{M_*} \frac{1}{G\Sigma_{\rm cloud}}$$
 (47a)

$$= 1.2\alpha_p \left(\frac{\Sigma_{\text{cloud}}}{10^3 \, M_{\odot} \, \text{pc}^{-2}} \right)^{-1}. \tag{47b}$$

The point at which ε_* is large enough that this inequality is satisfied is a simple estimate for the SFE needed to disperse the cloud, $\varepsilon_{*,\rm disp}$. For "normal" GMCs with $\Sigma_{\rm cloud} \sim 10^2\,M_{\odot}\,{\rm pc}^{-2}$, Equation (47b) reduces to

$$\varepsilon_{*,\text{disp}} \approx \frac{0.08}{\alpha_p} \frac{\Sigma_{\text{cloud}}}{10^2 \, M_{\odot} \, \text{pc}^{-2}}.$$
 (48)

For high surface density clouds $\Sigma_{\rm cloud} \sim 10^4 - 10^5 \, M_{\odot} \, {\rm pc}^{-2}$ such as those forming SSCs, this reduces to

$$1 - \varepsilon_{*,\text{disp}} \approx 0.06 \alpha_p \left(\frac{\Sigma_{\text{cloud}}}{10^4 \, M_{\odot} \, \text{pc}^{-2}} \right)^{-1}. \tag{49}$$

Clearly, extremely high surface densities would translate to an expected SFE very close to unity if winds were the only form of feedback acting. In the bottom right panel of Figure 4, we compare the estimate for $\varepsilon_{*,\mathrm{disp}}$ based on the EC solution with an equivalent calculation based on the Weaver et al. (1977) theory. Evidently, the loss of energy to cooling renders winds far less effective at limiting star formation in molecular clouds.

It is worth noting that Equation (47a) also applies in estimating the SFE for momentum sources other than winds, by substituting an alternative specific momentum input rate for $\alpha_p \dot{p}_w/M_*$. For example, for the same fully sampled Kroupa IMF (Kroupa 2001), SB99 gives a specific momentum injection rate from radiation of $L_*/(cM_*) \approx 20 \, \mathrm{km \, s^{-1} \, Myr^{-1}}$, a factor of 2.3 larger than the stellar wind momentum input rate in Equation (41) (see Figure 3). With $\alpha_p \sim 1$ –4 as obtained from our simulations (Paper II), the direct momentum input rates from radiation and winds would be comparable. Allowing for the combined momentum injection rate would respectively reduce the right-hand side of Equation (48) or increase the right-hand side of Equation (49) by a factor of \sim 2.

The above simple estimates of SFEs are interesting, but important caveats should be kept in mind. First, there is an implicit assumption that all wind momentum is retained in a cloud, but in fact it is likely that a significant portion is lost once the bubble size becomes comparable to that of the parent cloud, because the fractal bubble can break out through fingers and vent the shocked wind gas. For radiation feedback, estimates of the SFE based on the simple spherical assumption significantly underestimate the SFE obtained from simulations with realistic turbulent clouds owing to cancellation from multiple sources and escape through low-density channels (e.g., Raskutti et al. 2016; Dale 2017; Raskutti et al. 2017; Kim et al. 2018, 2019), and this is likely to be true for winds as well. Thus, Equations (48) and (49) should not be taken too seriously as direct predictions, but more properly as bracketing the potential impact of winds on ε_* .

Second, the effects of mass loss due to photoevaporation and ionized gas pressure acting on neutrals are not considered above. In fact, at low and moderate surface densities photoionization (and to a lesser extent direct radiation pressure) is quite effective in limiting star formation and dispersing clouds (e.g., Krumholz & Matzner 2009; Dale et al. 2012; Raskutti et al. 2016; Geen et al. 2017; Grudić et al. 2018; Kim et al. 2018, 2021; He et al. 2019). Our expectation is that stellar winds would aid in quenching star formation but are likely to rival the importance of photoevaporation only in clouds of quite high surface density (see Section 4).

Our results also provide an estimate for the thermal pressure of hot gas in the interior of the bubble, which is a key observable. Equation (21) gives the pressure as a function of bubble radius \mathcal{R}_b ; writing this in dimensional form, the result is

$$\frac{P_b}{k_{\rm B}} \approx 2.46 \times 10^6 \,\mathrm{K \, cm^{-3}} \frac{M_*}{10^3 \,M_\odot} \left(\frac{\mathcal{R}_b}{1 \,\mathrm{pc}}\right)^{-2} \frac{3\alpha_p - 1}{2}.$$
 (50)

In the bottom left panel of Figure 4, we compare the bubble pressure when $\mathcal{R}_b = R_{\text{cloud}}$ to the bubble pressure predicted by the Weaver et al. (1977) theory for several different cluster masses. It is striking that the pressures differ by two or three orders of magnitude over much of the parameter space.

Even with cooling losses, the pressure given by Equation (50) would be quite high for small bubbles powered by luminous, massive clusters. Larger bubbles around lower-mass clusters would have much more moderate pressure. For the wind bubbles around single O stars rather than stellar clusters, the predicted pressure in hot gas is

$$\frac{P_b}{k_{\rm B}} \approx 2.86 \times 10^5 \,\text{K cm}^{-3}
\times \frac{\dot{p}_{w,1}}{10^3 \,M_{\odot} \,\text{km s}^{-1} \,\text{Myr}^{-1}} \left(\frac{\mathcal{R}_b}{1 \,\text{pc}}\right)^{-2} \frac{3\alpha_p - 1}{2}, \quad (51)$$

where $\dot{p}_{w,1} = (2\dot{E}_{w,1}\dot{M}_{w,1})^{1/2}$ is the single-star wind momentum input rate.

For our simulations, as presented in Paper II (see Figures 1 and 2 there), the hot-gas pressure is far lower than that predicted in the original Weaver solution because most of the energy deposited by the wind is lost to cooling. Paper II shows that the measured energy reduction factor $1-\Theta\sim 0.1$ –0.01 is in good agreement with Equation (25). Taking $\mathcal{S}\approx \alpha_p$, the instantaneous fraction of the injected wind energy that is not radiated away is predicted to be

$$1 - \Theta \approx 4 \times 10^{-3} \alpha_p \frac{v_{\rm sh}}{10 \,\text{km s}^{-1}} \tag{52}$$

in terms of the shell's expansion velocity $v_{\rm sh} = \dot{\mathcal{R}}_b$. Even if this velocity is not measured directly, it may be estimated from other observables through Equation (43b).

The comparisons of this section between results obtained using the EC solution and the classical Weaver et al. (1977) solution show that neglect of energy losses due to interface mixing can lead to erroneous conclusions regarding the importance of stellar winds compared to other feedback mechanisms. For star clusters prior to breakout from molecular clouds, the EC conditions of this paper will generally apply, and we recommend use of formulae in this section. For a cluster after breakout or for runaway stars, the ambient density would be lower, leading to a longer cooling time t_{cool} . Lower power sources than the clusters of $M_* \gtrsim 10^3 \, M_\odot$ considered here would produce lower turbulent velocities v_t . In the longer- t_{cool} , smaller- v_t situations where interface energy losses are more moderate, we instead recommend use of the formulae in El-Badry et al. (2019) with an appropriate diffusion parameter (such as Equation (37)).

4. Discussion

4.1. Observations

This work was inspired in part by observations of evolved H II regions, which suggest that the classical model of Castor et al. (1975) and Weaver et al. (1977)—in which nearly half of the wind energy remains in a hot bubble that can emit X-rays and drive rapid shell expansion (\sim 10–50 km s⁻¹ from Figure 4)—is not in agreement with observations (Townsley et al. 2003, 2006; Harper-Clark & Murray 2009; Lopez et al. 2011, 2014; Rosen et al. 2014). Instead, observations suggest that wind energy must be lost either through leakage (Harper-Clark & Murray 2009) or through radiative cooling at intermediate temperatures. The former is encouraged by the highly inhomogeneous structure of clouds, while the latter is facilitated by turbulent mixing. We have explored the consequences of turbulent mixing and cooling as a major energy sink for shocked wind gas. In Paper II, we show that such extreme cooling is not only possible but also quite typical. These effects are expected to be especially important for early evolution before wind bubbles break out of their natal cloud. We have proposed (and show in Paper II) that the interfaces between hot and cool gas in wind bubbles are fractals; this is crucial in enhancing mixing and also important to breakout, as bubble "fingers" can vent gas earlier than would otherwise occur.

The EC model may be able to explain several observations. Rosen et al. (2014) showed that, for the four dense star clusters they studied, only 3%–30% of the energy deposited by stellar winds could be accounted for by radiative cooling internal to the bubble (negligible for the most part) combined with mechanical work on the surroundings (bottom left panels of Figures 6-9 in that work), suggesting that up to 97% of the wind energy is lost. While Rosen et al. (2014) were able to explain the missing energy in some of the clusters by appealing to thermal conduction (under the assumption that energy is lost, rather than leading to evaporation) and dust-reprocessed radiation, these calculations are more uncertain and sometimes overaccount for the lost energy. Rosen et al. (2014) also raised the possibility of significant energy losses by "turbulent conduction" (turbulent mixing+cooling in our terminology), but they did not attempt to estimate this. Since we find (see Paper II, Figure 17) that as little as 1% of the input energy remains in our simulation, we conclude that radiative cooling in

turbulent mixing layers would easily account for the missing wind energy in observed star-forming regions.

Olivier et al. (2021) recently observed deeply embedded H II regions, where our theory should be most applicable, but were only able to put upper limits on effects of stellar winds owing to a lack of long-exposure X-ray observations. Further work on this front should allow a quantitative test of our theory.

The nearby Orion Molecular Cloud has some of the best observations of ongoing star formation feedback in action. Using X-ray observations with the XMM-Newton satellite, Güdel et al. (2008) showed that the bubble being driven by the Trapezium cluster is pervaded by $(1.7-2.1) \times 10^6$ K gas and estimated an electron density $n_e = 0.2$ –0.5 cm⁻³, implying thermal pressure of $P_b/k_{\rm B} = 2n_e T = (0.68-2.1) \times 10^6 \ {\rm K \ cm^{-3}}.$ Using the wind parameters quoted for θ^1 Ori C (the most massive star in the Trapezium) by Güdel et al. (2008), $\dot{M}_{\rm w} = 0.8 \, M_{\odot} \, {\rm Myr^{-1}}$ and $\mathcal{V}_{\rm w} = 1650 \, {\rm km \, s^{-1}}$, we get $\dot{p}_{\rm w} =$ $1.32 \times 10^3 \, M_{\odot} \, \mathrm{km \, s^{-1} \, Myr^{-1}}$. Using Equation (51) and an effective radius of 2 pc (Güdel et al. 2008 suggest a range of 1-4 pc, uncertain owing to geometry), we find we would require $\alpha_p \approx 5$ to obtain pressure agreement at the lower end of the estimated range. This value of α_p is similar to the results we find in our simulations for our lowest momentum input rate, $\dot{p}_{\rm w}=1.8\times 10^4\,M_\odot~{\rm km~s^{-1}\,Myr^{-1}}$ (Paper II), considering the considerable uncertainties in the observational parameters; for example, substituting the estimated wind momentum input rate of Gagné et al. (2005) would increase the pressure by a factor of two.

Our work helps to explain why observational (listed above) and numerical (Dale et al. 2014; Geen et al. 2015a, 2021) works have found winds to be inefficient at cloud dispersal compared to effects from ionizing radiation. However, taking these results to mean that winds are unimportant is an oversimplification. Winds remain important not only because they pollute the gas surrounding nascent star clusters, perhaps changing the chemical composition of subsequent stellar populations (e.g., Bastian & Lardo 2018; Gratton et al. 2019), but also because they may be the primary mechanism for cloud dispersal *in some environments*.

Very recently, new empirical evidence of feedback in extreme environments was obtained by Levy et al. (2021), who observed the environment of nascent SSCs in NGC 253 with 0.5 pc resolution ALMA observations in multiple molecular lines. From analysis of P Cygni profiles, indicative of cluster-scale outflows, Levy et al. (2021) obtained estimates of the mass and momentum carried by outflows around three of the SSCs in NGC 253 and applied our theory of stellar wind feedback to test whether this could explain the observations. They found that given modest momentum enhancement factors, $\alpha_p \sim 1$ –4, winds could plausibly be the dominant feedback mechanism. However, our numerical findings (see Paper II, Figure 8) suggest that $\alpha_p \sim 1-1.5$ in the dense environments of SSCs (assuming high SFE). Given the uncertainty in the measurements, winds could still be the main drivers of feedback in these systems. The inferred $\alpha_p \gtrsim 2$ could, however, also be a sign of the contribution of other feedback mechanisms, such as radiation. A top-heavy IMF (see Figure 3) or a supersolar-metallicity (not shown) stellar population could also boost the input momentum/stellar mass (Leitherer et al. 1992; Vink et al. 2001; Leitherer et al. 2014).

4.2. Other Models of Momentum-driven Bubbles

In Section 3, we explicitly compared our results to what would be predicted based on the classic "Weaver-type" solution described in Section 2.1. This type of solution can be classified as "energy-driven" evolution because the energy of the bubble increases linearly in time, with the bubble radius expanding as $\mathcal{R}_b \propto t^{3/5}$. In contrast, in our EC solution it is the *momentum* that increases linearly in time, while energy only increases as the square root of time. Evolution in the EC solution may therefore be classified as "momentum driven."

Momentum-driven solutions for wind bubble expansion are characterized by $\mathcal{R}_b \propto t^{1/2}$ and have been considered by several previous authors. Steigman et al. (1975) simply assumed momentum-driven evolution, disregarding the importance of shocks and internal bubble structure. Avedisova (1972), Castor et al. (1975), and Weaver et al. (1977) clarified the role of internal wind shocks and argued for the importance of energy buildup within the bubble. Subsequent authors discussed the possibility of momentum-driven evolution due to enhanced cooling within the bubble interior, due to a variety of mechanisms described below. Two key differences of our theory from these earlier proposals are that (1) in our model energy is lost through strong radiative cooling at intermediate temperature in a turbulent mixing layer at the surface of the bubble, and (2) fractal structure of the interface is essential to efficient cooling.

The wind models of Koo & McKee (1992a, 1992b) specify a so-called "slow wind" that leads to momentum-driven bubble evolution. However, in this model the momentum-driven evolution is caused by the interior of the bubble being radiative when the wind is sufficiently dense and slow, where "slow" here is hundreds of kilometers per second, much slower than the $V_w > 10^3 \text{ km s}^{-1}$ winds under consideration in this paper.

Similarly, Section 7B of Ostriker & McKee (1988) considers that interior radiative losses could be enhanced owing to the evaporation of clouds overtaken by the wind (see Cowie & McKee 1977). In this scenario, the majority of the cooling would still occur in the shocked bubble interior.

In Silich & Tenorio-Tagle (2013) and Mac Low & McCray (1988) (following Weaver et al. 1977) it is emphasized that conduction acting at the boundary between the shocked wind and swept-up material creates a temperature gradient and includes a regime where cooling would be efficient, which would eventually lead to the evolution becoming momentum driven. This is the scenario most similar to our model. However, as discussed in Silich & Tenorio-Tagle (2013), for typical parameters this transition is only expected to occur after \sim 10 Myr, long past the timescales of evolution considered here or over which the wind can be treated as constant luminosity (as evidenced by Figure 3). In our model, radiative cooling in a turbulent mixing layer is far more efficient than the conductioninduced cooling, due in part to the fractal nature of the interface, and the bubble becomes momentum driven at much earlier times.

4.3. Comparison to Radiative Feedback

Several studies have argued analytically or demonstrated numerically that radiation feedback becomes much less efficient at dispersing clouds and limiting star formation in very high density environments (e.g., Fall et al. 2010; Dale et al. 2012; Kim et al. 2016, 2018; Raskutti et al. 2016;

Grudić et al. 2018; Rahner et al. 2019; Fukushima et al. 2020), even allowing for reprocessed radiation (Skinner & Ostriker 2015; Tsang & Milosavljević 2018). In such dense clouds, the evolutionary timescales are also too short for supernovae to be important in dispersing cloud material.

Quantitatively, Kim et al. (2018) (Figures 8 and 12) show that when the surface density of a cloud exceeds $\sim 10^3 \, M_\odot \, \mathrm{pc}^{-2}$, the total momentum injection rate per stellar mass due to EUV and far-UV radiation pressure⁶ drops below that in Equation (41) for winds. This suggests that winds could potentially be the dominant feedback process in higher-density environments. In particular, our theory may be able to explain several aspects of the extremely compact molecular clouds seen to be forming SSCs in nearby galaxies (Johnson et al. 2015; Oey et al. 2017; Turner et al. 2017; Leroy et al. 2018; Emig et al. 2020). As SSCs/young massive clusters (e.g., Whitmore 2003; Portegies Zwart et al. 2010) are the densest redshift-zero loci of star formation, understanding their formation not only is interesting in itself but also provides a window on globular cluster formation.

It may be noted that the linear dependence of ε_* on surface density given by Equation (48) is similar to the case of radiation-pressure-driven cloud dispersal under the idealization of a spherical system (Fall et al. 2010; Kim et al. 2016; see also Grudić et al. 2018; Li et al. 2019). This differs from the $\varepsilon_* \propto \Sigma_{\rm cloud}^{1/2}$ dependence reported by Fukushima et al. (2020). A relation $\varepsilon_* \propto \Sigma_{\mathrm{cloud}}^{1/2}$ is close to what would be predicted if the cloud lifetime scales linearly with the propagation time of a self-similarly expanding ionization front, while the star formation rate scales inversely with the cloud freefall time. However, the generality of the Fukushima et al. (2020) result may be questioned, since their simulations adopted very strongly self-gravitating clouds with a limited range of initial gas surface density. In contrast, the radiation-hydrodynamic simulations of Kim et al. (2018) found a non-power-law scaling of ε_* with Σ_{cloud} (see their Equation (26)) over a wider parameter range for clouds that were initially marginally bound. The difference between simple scaling predictions and full numerical results for the case of radiation-driven cloud destruction serves as a caution against taking Equation (47a) as more than a general indicator of the trend in SFE. Full numerical simulations will be needed to assess the effectiveness of winds in limiting star formation in clouds of varying conditions.

Regardless of the environment, winds may be more important than ionizing radiation at early stages of evolution when the radius of the H II region is small. Similar to the approach in Krumholz & Matzner (2009), one can make a simple comparison of the wind momentum input rate $\alpha_p \dot{p}_w$ to the nominal force imposed by thermal pressure of photoionized gas. For an effective bubble radius \mathcal{R}_b , the latter is $2n_e k_B T_{\rm II} (4\pi \mathcal{R}_b^2) \propto (Q_{\rm i} \mathcal{R}_b)^{1/2}$, where we have used $n_e = [3f_{\rm ion} Q_{\rm i}/(\alpha_B 4\pi \mathcal{R}_b^3)]^{1/2}$ for ionization equilibrium with a source of ionizing photon rate $Q_{\rm i}$ and a fraction $f_{\rm ion}$ of photons available for ionization, and $T_{\rm II}$ denotes the temperature of the photoionized gas. The force from the wind would exceed that from radiation when the radius is smaller than a

characteristic radius

$$\mathcal{R}_{b,\text{ch}} = \frac{\alpha_{\text{B}}}{12\pi (2k_{\text{B}}T_{\text{II}})^2} \frac{\alpha_p^2 \dot{p}_{\text{W}}^2}{f_{\text{for}} Q_{\text{i}}}.$$
 (53)

Adopting $T_{\rm II} = 8000 \, \text{K}$, $\alpha_{\rm B} = 3.03 \times 10^{-13} \, \text{cm}^3 \, \text{s}^{-1}$, and $f_{\rm ion} = 0.5$, the characteristic radius for a bubble driven by a single massive star with $\dot{p}_{\rm w} = 10^4 \, M_{\odot} \, \text{km s}^{-1} \, \text{Myr}^{-1}$ and $Q_{\rm i} = 4 \times 10^{49} \, \text{s}^{-1} \, \text{is} \, \mathcal{R}_{b, \rm ch} = 0.11 \alpha_p^2 \, \text{pc}$. For a star cluster with $Q_{\rm i} \approx 4 \times 10^{46} \, \text{s}^{-1} \, (M_*/M_{\odot})$ and $\dot{p}_{\rm w} = 8.6 \, \text{km s}^{-1} \, \text{Myr}^{-1} M_*$, we obtain $\mathcal{R}_{b, \rm ch} \approx 0.79 \alpha_p^2 (M_*/10^4 \, M_{\odot}) \, \text{pc}$; the wind is expected to play a greater role than photoionization for bubbles created by massive cluster stars in an early stage of evolution.

Therefore, similar to the situation analyzed by Kim et al. (2016), where the role of wind momentum input is played by radiation pressure, for sufficiently small radii it would be expected that the wind dominates the dynamics. The ionized gas layer would be compressed by the wind into a narrow layer near the ionization front. The wind would indirectly drive the shell expansion by enhancing density and thermal pressure of the HII region. The relative volumes of the hot-gas and photoionized-gas regions can be obtained by requiring that the pressures match. In the regime where winds dominate, radiation pressure is expected to contribute to the expansion by further increasing the density at the ionization front (Kim et al. 2016; Rahner et al. 2017). Later in evolution when the radius of the HII region is large, the photoionized gas would instead compress the hot interior of the bubble. Expansion would be driven primarily by photoionized gas that fills most of the bubble volume.

We note that the quantitative predictions above are based on the assumption that there is no significant leakage of hot gas and radiation. At a late stage of bubble evolution ($\mathcal{R}_b \sim R_{\text{cloud}}$), both (hot and photoionized) gas and radiation are expected to break out through low-density holes created by turbulence.

4.4. Other Physics

The theory presented here, as well as the simulations described in Paper II, are highly idealized, not considering many aspects of physical processes and the astronomical parameter space that could be important to the problem at hand. We briefly discuss some of these issues here.

First, the relevance of our results may be metallicity dependent. We note that wind mass loss is almost linear with metallicity, $d \log \dot{M}_{\rm w}/d \log Z \sim 0.7$, while the wind velocity has a weak dependence on metallicity ($V_{\rm w} \propto Z^{0.13}$), so that the wind momentum input rate is almost linear in metallicity (Vink et al. 2001). Lower metallicity in the cloud could in principle also make cooling less effective. However, we show in Paper II that most cooling in the turbulently mixed interface gas occurs near $T \sim 10^4$ K, where cooling is mostly due to hydrogen (Ly α), implying that a change in metallicity should not have a strong effect. Therefore, the effect of winds is expected to decrease at lower metallicity.

Second, we ignore thermal conduction. As noted above and in El-Badry et al. (2019), thermal conduction can act to increase the density and decrease the temperature of the bubble interior at fixed pressure. While it is not known whether the effect of thermal conduction in the presence of genuine turbulent mixing acts the same as for a parameterized

⁶ From Figure 7 of Kim et al. (2018), direct radiation pressure dominates over effects of photoevaporation and ionized gas pressure in this regime.

diffusivity, if this is the case, we might still expect the thermal pressure to follow Equations (50) and (51).

Finally, while we do not include magnetic fields in our models, in general we would expect them to have at least two effects. First, they would add to the external pressure and tension that the bubble must "fight against" to expand. However, our power-law solutions already neglect external turbulent and thermal stresses; when accounted for, these and the magnetic stresses would slow expansion when $\dot{p}_{\rm w}/(4\pi R_b^2)$ becomes comparable to the total external stress (and depending on the field geometry, the bubble may also expand preferentially along the field lines). Second, a magnetic field could act to inhibit development of the turbulent mixing that leads to cooling. For example, the Kelvin-Helmholtz instability is suppressed if the Alfvén speed in the shell gas exceeds $v_{\rm shear}/\chi^{1/2}$, where $v_{\rm shear}$ is the shear velocity and χ is the ratio between the density of shell gas and shocked wind gas. Even if primary instabilities take place, magnetic tension may limit turbulent cascades to small scales. Also, inclusion of radiation, as discussed above, would imply that the hot gas may principally interact with a layer of photoevaporated gas rather than directly with the shell gas. Numerical study will be needed to assess the parameter regime where the mixing/cooling process and bubble evolution are strongly affected.

5. Conclusion

We have presented a theory for stellar wind bubble evolution with extremely efficient energy losses to radiative cooling, such that bubble expansion is determined by the original wind momentum injection rate. In this theoretical model, the extreme energy losses are the result of turbulent mixing and subsequent radiative cooling at the interface between hot and cool gas at the bubble surface, strongly enhanced by the large interface area that arises from the fractal geometry of the bubble.

In a companion paper, referred to throughout this work as Paper II, we validate our theory using three-dimensional hydrodynamic simulations of wind-driven bubble evolution, demonstrating excellent agreement. In Paper II we quantify the few free parameters of our theory and provide a full analysis of thermal and dynamical structure and evolution.

The treatment of stellar winds in this paper and its companion has been largely simplified (constant luminosity with central point-like star clusters put in by hand). This treatment allowed us to gain a deeper theoretical understanding of the stellar wind bubble physics that controls evolution. Still, a fully self-consistent treatment of star formation with wind feedback for a range of cloud parameters—both normal GMCs and clouds capable of forming SSCs—remains an important goal. The fractal theory developed here will serve as a valuable tool aiding interpretation in this kind of numerical effort, as well as observational studies of star-forming cloud structure and evolution. In addition, the theory developed here may potentially be applied to understanding the history of chemical enrichment of natal clouds by embedded clusters, which would illuminate many long-standing problems involving multiple stellar populations within globular clusters (e.g., Lochhaas & Thompson 2017; Wünsch et al. 2017; Bastian & Lardo 2018; Gratton et al. 2019).

We thank Drummond Fielding and Erin Kado-Fong for useful discussions. We thank the referee for their many insightful comments that improved the quality of the manuscript. We thank

Cameron Lancaster for the production of the schematics shown in Figure 1. This work was partly supported by the National Science Foundation (AARG award AST-1713949) and NASA (ATP grant No. NNX17AG26G). J.-G.K. acknowledges support from the Lyman Spitzer Jr. Postdoctoral Fellowship at Princeton University. Computational resources were provided by the Princeton Institute for Computational Science and Engineering (PICSciE) and the Office of Information Technology's High Performance Computing Center at Princeton University.

Software: scipy (Virtanen et al. 2020), numpy (Harris et al. 2020), matplotlib (Hunter 2007), adstex (https://github.com/yymao/adstex).

Appendix The Wind Interior

Here we provide a derivation for some of the properties of the free and shocked wind phases. This analysis allows us to write the energy enhancement factor S, post-shock pressure, and the relative volume of free and shocked wind in terms of a "momentum enhancement factor" α_p .

We assume spherical geometry for the bubble with $r < \mathcal{R}_{\rm f}$ occupied by the free wind phase, where $\mathcal{R}_{\rm f} = (3V_{\rm f}/4\pi)^{1/3}$ for the volume $V_{\rm f}$ occupied by the free wind and $\mathcal{R}_{\rm f} < r < \mathcal{R}_b$ occupied by shocked wind gas.

In the free wind the flow expands with hypersonic wind velocity \mathcal{V}_w and the thermal energy is negligible, so that

$$\rho(r) = \frac{\dot{M}_{\rm w}}{4\pi r^2 \mathcal{V}_{\rm w}} , \quad v_r = \mathcal{V}_{\rm w}. \tag{A1}$$

At \mathcal{R}_f the wind then goes through a strong shock (assumed perpendicular), with immediate post-shock conditions

$$\rho_{\rm ps} = 4\rho(\mathcal{R}_{\rm f}) = \frac{\dot{M}_{\rm w}}{\pi \mathcal{R}_{\rm f}^2 \mathcal{V}_{\rm w}},\tag{A2}$$

$$v_{\rm ps} = \frac{\mathcal{V}_{\rm w}}{4},\tag{A3}$$

and

$$P_{\rm ps} = 3\rho_{\rm ps}v_{\rm ps}^2 = \frac{3\dot{p}_{\rm w}}{16\pi\mathcal{R}_{\rm f}^2}.$$
 (A4)

The shocked wind region is assumed to have a steady flow,

$$\frac{\rho}{\rho_{\rm ps}} = \frac{\mathcal{R}_{\rm f}^2 \, v_{\rm ps}}{r^2 \, v},\tag{A5}$$

with an adiabatic equation of state,

$$\frac{P}{\rho} = \frac{P_{\rm ps}}{\rho_{\rm ps}} \left(\frac{\rho}{\rho_{\rm ps}}\right)^{2/3},\tag{A6}$$

and Bernoulli parameter

$$\frac{1}{2}v^2 + \frac{5}{2}\frac{P}{\rho} = \frac{1}{2}v_{\rm ps}^2 + \frac{5}{2}\frac{P_{\rm ps}}{\rho_{\rm ps}}.$$
 (A7)

By substituting in for P and ρ in the Bernoulli equation, we obtain

$$\left(\frac{v}{v_{\rm ps}}\right)^2 + 15\left(\frac{v_{\rm ps}}{v}\left(\frac{\mathcal{R}_{\rm f}}{r}\right)^2\right)^{2/3} = 16,\tag{A8}$$

which can be rearranged to arrive at

$$\frac{v}{v_{\rm ps}} = \left(\frac{\mathcal{R}_{\rm f}}{r}\right)^2 \left(\frac{15}{16 - (v/v_{\rm ps})^2}\right)^{3/2}.$$
 (A9)

While this equation does have an analytic solution, it is quite complicated; an approximation that is good to within 10% is

$$\frac{v}{v_{\rm ps}} \approx \left(\frac{\mathcal{R}_{\rm f}}{r}\right)^2$$
 (A10)

With Equation (A10), both the density and pressure are approximately constant throughout the post-shock region, equal to their immediate post-shock values given in Equations (A2) and (A4), $\rho = \rho_{\rm ps}$ and $P = P_{\rm ps}$.

The total rate of momentum transport across a surface of radius r is

$$\dot{p}(r) = 4\pi r^2 (P + \rho v^2),$$

which in the free wind region is $\dot{p}(r) = \dot{p}_{w}$. Using our solution in the shocked wind region, this becomes

$$\dot{p}(r) = \frac{\dot{p}_{w}}{4} \left[3 \left(\frac{r}{\mathcal{R}_{f}} \right)^{2} + \left(\frac{r}{\mathcal{R}_{f}} \right)^{-2} \right]. \tag{A11}$$

This function is strictly increasing for $r/\mathcal{R}_f > 1$.

The total momentum input to the shell is obtained by taking $r \to \mathcal{R}_b$, which from the definition in Equation (13) implies

$$\alpha_p = \frac{1}{4} \left[3 \left(\frac{\mathcal{R}_b}{\mathcal{R}_f} \right)^2 + \left(\frac{\mathcal{R}_b}{\mathcal{R}_f} \right)^{-2} \right]. \tag{A12}$$

We can invert to obtain $\mathcal{R}_b/\mathcal{R}_f$ in terms of α_p as

$$\left(\frac{\mathcal{R}_b}{\mathcal{R}_f}\right)^2 = \frac{2}{3}\alpha_p + \left[\left(\frac{2}{3}\alpha_p\right)^2 - \frac{1}{3}\right]^{1/2}.$$
 (A13)

A useful and simple approximation for the above, which is good to within 4% for $1 \le \alpha_n \le 4$, is given by

$$\left(\frac{\mathcal{R}_b}{\mathcal{R}_f}\right)^2 \approx \frac{1}{2}(3\alpha_p - 1);$$
 (A14)

alternatively, at large α_p , $(\mathcal{R}_b/\mathcal{R}_f)^2 \approx 4\alpha_p/3$. The free wind's volume is a fraction $(\mathcal{R}_b/\mathcal{R}_f)^{-3}$ of the whole wind bubble.

Finally, under the assumption of spherical symmetry, the total energy in the bubble interior is

$$E_b = 4\pi \int_0^{\mathcal{R}_b} \left(\frac{3}{2} P + \frac{1}{2} \rho v^2 \right) r^2 dr.$$

Given that only the kinetic energy term contributes in the free wind, we can use Equation (A1) to derive the total energy in the free wind as $\dot{p}_{\rm w} \mathcal{R}_{\rm f}/2$. For the shocked wind we can derive the energy as

$$E_{\rm ps} = \frac{\dot{p}_{\rm w} \mathcal{R}_{\rm f}}{8} \left[3 \left(\frac{\mathcal{R}_b}{\mathcal{R}_{\rm f}} \right)^3 - 2 - \frac{\mathcal{R}_{\rm f}}{\mathcal{R}_b} \right].$$

Putting these together, the total energy in the bubble interior is

$$E_b = \frac{\dot{p}_{\rm w} \mathcal{R}_b \mathcal{S}}{2},\tag{A15}$$

where

$$S = \frac{3}{4} \left(\frac{\mathcal{R}_b}{\mathcal{R}_f}\right)^2 - \frac{1}{4} \left(\frac{\mathcal{R}_b}{\mathcal{R}_f}\right)^{-2} + \frac{1}{2} \left(\frac{\mathcal{R}_b}{\mathcal{R}_f}\right)^{-1} \tag{A16}$$

is the enhancement in energy above the case where the whole wind bubble is made up of free wind ($\mathcal{R}_b = \mathcal{R}_f$ and $\mathcal{S} = 1$). Using Equation (A12), one can show that $\mathcal{S} \approx \alpha_p$ to within 6%.

We note that to account for the shock between the free and post-shock wind being oblique, Equation (A3) can be multiplied by a factor $4-3\mu^2$ to obtain the post-shock radial velocity, while for the post-shock pressure Equation (A4) is multiplied by μ^2 . Here μ is the average value of the dot product of the unit radial vector ($\hat{\bf r}$) with the unit normal to the shock ($\hat{\bf n}_{\rm shock}$).

ORCID iDs

Lachlan Lancaster https://orcid.org/0000-0002-0041-4356 Eve C. Ostriker https://orcid.org/0000-0002-0509-9113 Jeong-Gyu Kim https://orcid.org/0000-0001-6228-8634 Chang-Goo Kim https://orcid.org/0000-0003-2896-3725

References

Avedisova, V. S. 1972, SvA, 15, 708

Badjin, D. A., Glazyrin, S. I., Manukovskiy, K. V., & Blinnikov, S. I. 2016, MNRAS, 459, 2188

Bally, J. 2016, ARA&A, 54, 491

Barnes, A. T., Longmore, S. N., Battersby, C., et al. 2017, MNRAS, 469, 2263 Barnes, A. T., Longmore, S. N., Dale, J. E., et al. 2020, MNRAS, 498, 4906 Bastian, N., & Lardo, C. 2018, ARA&A, 56, 83

Blondin, J. M., Wright, E. B., Borkowski, K. J., & Reynolds, S. P. 1998, ApJ, 500, 342

Bucciantini, N., Amato, E., Bandiera, R., Blondin, J. M., & Del Zanna, L. 2004, A&A, 423, 253

Capriotti, E. R., & Kozminski, J. F. 2001, PASP, 113, 677

Castor, J., McCray, R., & Weaver, R. 1975, ApJL, 200, L107

Chevance, M., Kruijssen, J. M. D., Krumholz, M. R., et al. 2020a, arXiv:2010.

Chevance, M., Kruijssen, J. M. D., Vazquez-Semadeni, E., et al. 2020b, SSRv, 216, 50

Cowie, L. L., & McKee, C. F. 1977, ApJ, 211, 135

Dale, J. E. 2017, MNRAS, 467, 1067

Dale, J. E., Ercolano, B., & Bonnell, I. A. 2012, MNRAS, 424, 377

Dale, J. E., Ngoumou, J., Ercolano, B., & Bonnell, I. A. 2014, MNRAS, 442, 694

Dunne, B. C., Chu, Y.-H., Chen, C. H. R., et al. 2003, ApJ, 590, 306 El-Badry, K., Ostriker, E. C., Kim, C.-G., Quataert, E., & Weisz, D. R. 2019,

MNRAS, 490, 1961

Emig, K. L., Bolatto, A. D., Leroy, A. K., et al. 2020, ApJ, 903, 50 Evans, N. J., I., Dunham, M. M., Jørgensen, J. K., et al. 2009, ApJS, 181, 321

Fall, S. M., Krumholz, M. R., & Matzner, C. D. 2010, ApJL, 710, L142

Fielding, D. B., Ostriker, E. C., Bryan, G. L., & Jermyn, A. S. 2020, ApJL, 894, L24

Folini, D., & Walder, R. 2006, A&A, 459, 1

Franco, J., Shore, S. N., & Tenorio-Tagle, G. 1994, ApJ, 436, 795

Fukushima, H., Yajima, H., Sugimura, K., et al. 2020, MNRAS, 497, 3830

Gagné, M., Oksala, M. E., Cohen, D. H., et al. 2005, ApJ, 628, 986 Garcia-Segura, G., Langer, N., & Mac Low, M. M. 1996, A&A, 316, 133

Gatto, A., Walch, S., Naab, T., et al. 2017, MNRAS, 466, 1903

Geen, S., Bieri, R., Rosdahl, J., & de Koter, A. 2021, MNRAS, 501, 1352

Geen, S., Hennebelle, P., Tremblin, P., & Rosdahl, J. 2015a, MNRAS, 454, 4484

Geen, S., Rosdahl, J., Blaizot, J., Devriendt, J., & Slyz, A. 2015b, MNRAS, 448, 3248

Geen, S., Soler, J. D., & Hennebelle, P. 2017, MNRAS, 471, 4844 Girichidis, P., Offner, S. S. R., Kritsuk, A. G., et al. 2020, SSRv, 216, 68 Gratton, R., Bragaglia, A., Carretta, E., et al. 2019, A&ARv, 27, 8 Gronke, M., & Oh, S. P. 2018, MNRAS, 480, L111

This is always the case; see Paper II and Figure 1(b).

```
Grudić, M. Y., Hopkins, P. F., Faucher-Giguère, C.-A., et al. 2018, MNRAS,
   475, 3511
Güdel, M., Briggs, K. R., Montmerle, T., et al. 2008, Sci, 319, 309
Haid, S., Walch, S., Seifried, D., et al. 2018, MNRAS, 478, 4799
Harper-Clark, E., & Murray, N. 2009, ApJ, 693, 1696
Harris, C. R., Jarrod Millman, K., van der Walt, S. J., et al. 2020, Natur,
   585, 357
He, C.-C., Ricotti, M., & Geen, S. 2019, MNRAS, 489, 1880
Hennebelle, P., & Iffrig, O. 2014, A&A, 570, A81
Hosek, M. W., J., Lu, J. R., Anderson, J., et al. 2019, ApJ, 870, 44
Hunter, J. D. 2007, CSE, 9, 90
Johnson, K. E., Leroy, A. K., Indebetouw, R., et al. 2015, ApJ, 806, 35
Kennicutt, R. C., J. 1998, ARA&A, 36, 189
Kim, C.-G., & Ostriker, E. C. 2017, ApJ, 846, 133
Kim, C.-G., Ostriker, E. C., & Kim, W.-T. 2013, ApJ, 776, 1
Kim, C.-G., Ostriker, E. C., & Raileanu, R. 2017, ApJ, 834, 25
Kim, J.-G., Kim, W.-T., & Ostriker, E. C. 2016, ApJ, 819, 137
Kim, J.-G., Kim, W.-T., & Ostriker, E. C. 2018, ApJ, 859, 68
Kim, J.-G., Kim, W.-T., & Ostriker, E. C. 2019, ApJ, 883, 102
Kim, J.-G., Ostriker, E. C., & Filippova, N. 2021, ApJ, 911, 128
Klein, R. I., McKee, C. F., & Colella, P. 1994, ApJ, 420, 213
Koo, B.-C., & McKee, C. F. 1992a, ApJ, 388, 93
Koo, B.-C., & McKee, C. F. 1992b, ApJ, 388, 103
Kroupa, P. 2001, MNRAS, 322, 231
Kruijssen, J. M. D., Schruba, A., Chevance, M., et al. 2019, Natur, 569, 519
Krumholz, M. R., & Matzner, C. D. 2009, ApJ, 703, 1352
Krumholz, M. R., McKee, C. F., & Bland-Hawthorn, J. 2019, ARA&A,
   57, 227
Krumholz, M. R., & Tan, J. C. 2007, ApJ, 654, 304
Lada, C. J., Lombardi, M., & Alves, J. F. 2010, ApJ, 724, 687
Lancaster, L., Ostriker, E. C., Kim, J.-G., & Kim, C.-G. 2021, ApJ, 914, 90
Lee, E. J., Miville-Deschênes, M.-A., & Murray, N. W. 2016, ApJ, 833, 229
Leitherer, C., Ekström, S., Meynet, G., et al. 2014, ApJS, 212, 14
Leitherer, C., Robert, C., & Drissen, L. 1992, ApJ, 401, 596
Leitherer, C., Schaerer, D., Goldader, J. D., et al. 1999, ApJS, 123, 3
Leroy, A. K., Bolatto, A. D., Ostriker, E. C., et al. 2018, ApJ, 869, 126
Leroy, A. K., Schinnerer, E., Hughes, A., et al. 2017, ApJ, 846, 71
Levy, R. C., Bolatto, A. D., Leroy, A. K., et al. 2021, ApJ, 912, 4
Li, H., Vogelsberger, M., Marinacci, F., & Gnedin, O. Y. 2019, MNRAS,
   487, 364
Lochhaas, C., & Thompson, T. A. 2017, MNRAS, 470, 977
Lopez, L. A., Krumholz, M. R., Bolatto, A. D., et al. 2014, ApJ, 795, 121
Lopez, L. A., Krumholz, M. R., Bolatto, A. D., Prochaska, J. X., &
  Ramirez-Ruiz, E. 2011, ApJ, 731, 91
Lu, J. R., Do, T., Ghez, A. M., et al. 2013, ApJ, 764, 155
Mac Low, M.-M., & McCray, R. 1988, ApJ, 324, 776
Mackey, J., Gvaramadze, V. V., Mohamed, S., & Langer, N. 2015, A&A,
   573, A10
Matzner, C. D. 2002, ApJ, 566, 302
Matzner, C. D., & McKee, C. F. 2000, ApJ, 545, 364
McCrady, N., Graham, J. R., & Vacca, W. D. 2005, ApJ, 621, 278
```

McCray, R., & Kafatos, M. 1987, ApJ, 317, 190

```
McLeod, A. F., Dale, J. E., Evans, C. J., et al. 2019, MNRAS, 486, 5263
McLeod, A. F., Kruijssen, J. M. D., Weisz, D. R., et al. 2020, ApJ, 891, 25
Michaut, C., Cavet, C., Bouquet, S. E., Roy, F., & Nguyen, H. C. 2012, ApJ,
Murray, N. 2011, ApJ, 729, 133
Murray, N., Quataert, E., & Thompson, T. A. 2010, ApJ, 709, 191
Ntormousi, E., Burkert, A., Fierlinger, K., & Heitsch, F. 2011, ApJ, 731, 13
Oey, M. S., Herrera, C. N., Silich, S., et al. 2017, ApJL, 849, L1
Offner, S. S. R., & Chaban, J. 2017, ApJ, 847, 104
Olivier, G. M., Lopez, L. A., Rosen, A. L., et al. 2021, ApJ, 908, 68
Ostriker, J. P., & McKee, C. F. 1988, RvMP, 60, 1
Pellegrini, E. W., Baldwin, J. A., & Ferland, G. J. 2011, ApJ, 738, 34
Pittard, J. M. 2013, MNRAS, 435, 3600
Portegies Zwart, S. F., McMillan, S. L. W., & Gieles, M. 2010, ARA&A,
Rahner, D., Pellegrini, E. W., Glover, S. C. O., & Klessen, R. S. 2017,
   MNRAS, 470, 4453
Rahner, D., Pellegrini, E. W., Glover, S. C. O., & Klessen, R. S. 2019,
  MNRAS, 483, 2547
Raskutti, S., Ostriker, E. C., & Skinner, M. A. 2016, ApJ, 829, 130
Raskutti, S., Ostriker, E. C., & Skinner, M. A. 2017, ApJ, 850, 112
Rogers, H., & Pittard, J. M. 2013, MNRAS, 431, 1337
Rosen, A. L., Lopez, L. A., Krumholz, M. R., & Ramirez-Ruiz, E. 2014,
  MNRAS, 442, 2701
Sano, T., Nishihara, K., Matsuoka, C., & Inoue, T. 2012, ApJ, 758, 126
Scannapieco, E., & Brüggen, M. 2015, ApJ, 805, 158
Schneider, E. E., & Robertson, B. E. 2017, ApJ, 834, 144
Silich, S., & Tenorio-Tagle, G. 2013, ApJ, 765, 43
Skinner, M. A., & Ostriker, E. C. 2015, ApJ, 809, 187
Steigman, G., Strittmatter, P. A., & Williams, R. E. 1975, ApJ, 198, 575
Tan, B., Oh, S. P., & Gronke, M. 2021, MNRAS, 502, 3179
Thompson, T. A., Quataert, E., & Murray, N. 2005, ApJ, 630, 167
Toalá, J. A., & Arthur, S. J. 2018, MNRAS, 478, 1218
Townsley, L. K., Broos, P. S., Chu, Y.-H., et al. 2011, ApJS, 194, 16
Townsley, L. K., Broos, P. S., Feigelson, E. D., et al. 2006, AJ, 131, 2140
Townsley, L. K., Feigelson, E. D., Montmerle, T., et al. 2003, ApJ, 593, 874
Tsang, B. T. H., & Milosavljević, M. 2018, MNRAS, 478, 4142
Turner, J. L., Consiglio, S. M., Beck, S. C., et al. 2017, ApJ, 846, 73
Utomo, D., Sun, J., Leroy, A. K., et al. 2018, ApJL, 861, L18
Vink, J. S., de Koter, A., & Lamers, H. J. G. L. M. 2001, A&A, 369, 574
Virtanen, P., Gommers, R., Oliphant, T. E., et al. 2020, NatMe, 17, 261
Vishniac, E. T. 1983, ApJ, 274, 152
Vishniac, E. T. 1994, ApJ, 428, 186
Vishniac, E. T., & Ryu, D. 1989, ApJ, 337, 917
Vutisalchavakul, N., Evans, N. J., I., Heyer, M., et al. 2016, ApJ, 831, 73
Weaver, R., McCray, R., Castor, J., Shapiro, P., & Moore, R. 1977, ApJ,
  218, 377
Whitmore, B. C. 2003, in Proc. ESO Workshop, Extragalactic Globular Cluster
  Systems, ed. M. Kissler-Patig (New York: Springer), 336
Whitworth, A. 1979, MNRAS, 186, 59
Wolfire, M. G., & Cassinelli, J. P. 1987, ApJ, 319, 850
Wünsch, R., Palouš, J., Tenorio-Tagle, G., & Ehlerová, S. 2017, ApJ, 835, 60
```